

1 **Relating geostationary satellite measurements of aerosol optical**
2 **depth (AOD) over East Asia to fine particulate matter (PM_{2.5}):**
3 **insights from the KORUS-AQ aircraft campaign and GEOS-**
4 **Chem model simulations**

5 Shixian Zhai¹, Daniel J. Jacob¹, Jared F. Brewer¹, Ke Li¹, Jonathan M. Moch¹, Jhoon Kim^{2,3},
6 Seoyoung Lee², Hyunkwang Lim², Hyun Chul Lee³, Su Keun Kuk³, Rokjin J. Park⁴, Jaemin I.
7 Jeong⁴, Xuan Wang⁵, Pengfei Liu⁶, Gan Luo⁷, Fangqun Yu⁷, Jun Meng^{8, a}, Randall V. Martin⁸,
8 Katherine R. Travis⁹, Johnathan W. Hair⁹, Bruce E. Anderson⁹, Jack E. Dibb¹⁰, Jose L.
9 Jimenez¹¹, Pedro Campuzano-Jost¹¹, Benjamin A. Nault^{11, b}, Jung-Hun Woo¹², Younha Kim¹³,
10 Qiang Zhang¹⁴, Hong Liao¹⁵

11 ¹Harvard John A. Paulson School of Engineering and Applied Sciences, Harvard University, Cambridge, MA, USA

12 ²Department of Atmospheric Sciences, Yonsei University, Seoul, Republic of Korea

13 ³Samsung Particulate Matter Research Institute, Samsung Advanced Institute of Technology, 130 Samsung-ro,
14 Yeongtong-gu, Suwon-si, Gyeonggi-do, Republic of Korea

15 ⁴School of Earth and Environmental Sciences, Seoul National University, Seoul, Republic of Korea

16 ⁵School of Energy and Environment, City University of Hong Kong, Hong Kong SAR, China

17 ⁶School of Earth and Atmospheric Sciences, Georgia Institute of Technology, Atlanta, GA, USA

18 ⁷Atmospheric Sciences Research Center, University at Albany, Albany, New York, USA

19 ⁸Department of Energy, Environmental & Chemical Engineering, Washington University in St Louis, MO, USA

20 ⁹NASA Langley Research Center, Hampton, VA, USA

21 ¹⁰Institute for the Study of Earth, Oceans, and Space, University of New Hampshire, Durham, NH, USA

22 ¹¹Department of Chemistry, and Cooperative Institute for Research in Environmental Sciences, University of
23 Colorado, Boulder, CO, USA

24 ¹²Department of Civil and Environmental Engineering, Konkuk University, Seoul, Republic of Korea

25 ¹³International Institute for Applied Systems Analysis (IIASA), 2361 Laxenburg, Austria

26 ¹⁴Department of Earth System Science, Tsinghua University, Beijing, China.

27 ¹⁵Jiangsu Key Laboratory of Atmospheric Environment Monitoring and Pollution Control, Collaborative Innovation
28 Center of Atmospheric Environment and Equipment Technology, School of Environmental Science and
29 Engineering, Nanjing University of Information Science and Technology, Nanjing, China.

30 ^a Now at Department of Atmospheric & Oceanic Sciences, University of California, Los Angeles, California, USA

31 ^b Now at Center for Aerosol and Cloud Chemistry, Aerodyne Research, Inc., Billerica, MA, USA

32 *Correspondence:* Shixian Zhai (zhaisx@g.harvard.edu)

33

34 **Abstract.** Geostationary satellite measurements of aerosol optical depth (AOD) over East Asia from the GOCI and
35 AHI instruments can augment surface monitoring of fine particulate matter (PM_{2.5}) air quality, but this requires
36 better understanding of the AOD-PM_{2.5} relationship. Here we use the GEOS-Chem chemical transport model to
37 analyze the critical variables determining the AOD-PM_{2.5} relationship over East Asia by simulation of observations
38 from satellite, aircraft, and ground-based datasets. This includes the detailed vertical aerosol profiling over South
39 Korea from the KORUS-AQ aircraft campaign (May-June 2016) with concurrent ground-based PM_{2.5} composition,
40 PM₁₀, and AERONET AOD measurements. The KORUS-AQ data show that 550 nm AOD is mainly contributed by
41 sulfate-nitrate-ammonium (SNA) and organic aerosols in the planetary boundary layer (PBL), despite large dust
42 concentrations in the free troposphere, reflecting the optically effective size and high hygroscopicity of the PBL
43 aerosols. We updated SNA and organic aerosol size distributions in GEOS-Chem to represent aerosol optical
44 properties over East Asia by using in-situ measurements of particle size distributions from KORUS-AQ. We find
45 that SNA and organic aerosols over East Asia have larger size (number median radius of 0.11 μm with geometric
46 standard deviation of 1.4) and 20% larger mass extinction efficiency as compared to aerosols over North America
47 (default setting in GEOS-Chem). Although GEOS-Chem is successful in reproducing the KORUS-AQ vertical
48 profiles of aerosol mass, its ability to link AOD to PM_{2.5} is limited by under-accounting of coarse PM and by a large
49 overestimate of nighttime PM_{2.5} nitrate. The GOCI/AHI AOD data over East Asia in different seasons show
50 agreement with AERONET AODs and a spatial distribution consistent with surface PM_{2.5} network data. The AOD
51 observations over North China show a summer maximum and winter minimum, opposite in phase to surface PM_{2.5}.
52 This is due to low PBL depths compounded by high residential coal emissions in winter, and high relative humidity
53 (RH) in summer. Seasonality of AOD and PM_{2.5} over South Korea is much weaker, reflecting weaker variation of
54 PBL depth and lack of residential coal emissions.

55 **1 Introduction**

56 PM_{2.5} (particulate matter with aerodynamic diameter less than 2.5 μm) in surface air is a severe public health
57 concern in East Asia, but surface monitoring networks are too sparse to thoroughly assess population exposure.
58 Satellite observations of aerosol optical depth (AOD) can provide a valuable complement (Van Donkelaar et al.,
59 2015). Geostationary satellite sensors, including the Geostationary Ocean Color Imager (GOCI) launched by the
60 Korea Aerospace Research Institute (KARI) in 2011 (Choi et al., 2016, 2018, 2019) and the Advanced Himawari
61 Imager (AHI) launched by the Japanese Meteorological Agency (JMA) in 2014 (Lim et al., 2018, 2021), offer the
62 potential for high-density mapping of PM_{2.5} over East Asia. However, more confidence is needed in relating AOD to
63 PM_{2.5}. Here we evaluate the capability of the GEOS-Chem chemical transport model (CTM) to simulate AOD-PM_{2.5}
64 relationships over East Asia, exploiting in-situ aircraft measurements of vertical aerosol profiles and optical
65 properties from the joint NASA-NIER Korea - United States Air Quality (KORUS-AQ) field study in May-June
66 2016 (Crawford et al., 2021; Peterson et al., 2019; Jordan et al., 2020) together with GOCI/AHI geostationary
67 satellite data and surface measurement networks. This enables us to identify critical variables and uncertainties for
68 inferring PM_{2.5} from satellite AOD data.

69 A number of past studies have used satellite AOD data to infer surface $PM_{2.5}$ using physical and statistical models.
70 The standard geophysical approach has been to use a CTM, such as GEOS-Chem, to compute the $PM_{2.5}/AOD$ ratio
71 (Liu et al., 2004; van Donkelaar et al., 2006; van Donkelaar et al., 2015; Xu et al., 2015; Geng et al., 2017), with
72 recent applications correcting for CTM biases using available $PM_{2.5}$ surface network data (Brauer et al., 2016; Van
73 Donkelaar et al., 2016; van Donkelaar et al., 2019; Hammer et al., 2020). An alternative approach is to use machine-
74 learning algorithms to relate satellite AOD to $PM_{2.5}$ by training on the surface network data (Hu et al., 2017; Chen et
75 al., 2018; Xiao et al., 2018; Wei et al., 2021; Pendergrass et al., 2021), and sometimes including CTM values as
76 predictors (Di et al., 2019; Xue et al., 2019). Yet another approach is to assimilate the satellite-measured AODs in a
77 CTM and correct in this manner the $PM_{2.5}$ simulation, although this requires attribution of model AOD errors to
78 specific model parameters (Kumar et al., 2019; Saide et al., 2014; Sekiyama et al., 2010; Cheng et al., 2019). In all
79 of these approaches, a better physical understanding of the AOD- $PM_{2.5}$ relationship as simulated by CTMs can
80 greatly enhance the capability to infer $PM_{2.5}$ from AOD data.

81 AOD measures aerosol extinction (scattering and absorption) integrated over the atmospheric column, so that its
82 relationship to 24-hr average surface $PM_{2.5}$ (the standard air quality metric) depends on the aerosol vertical
83 distribution and optical properties, ambient relative humidity (RH), diurnal variation of $PM_{2.5}$, and contribution from
84 coarse particulate matter to AOD. Little study of these factors has been conducted for East Asia. Airborne
85 measurements of aerosol vertical profiles in East Asia are very limited (Liu et al., 2009; Sun et al., 2013). AOD is
86 highly sensitive to RH (Brock et al., 2016; Latimer and Martin et al., 2019; Saide et al., 2020), but the impact from
87 RH uncertainty on AOD simulation lacks evaluation. In addition, because the AOD is a daytime measurement that
88 needs to be related to 24-h average $PM_{2.5}$, the diurnal variation of $PM_{2.5}$ needs to be understood (Guo et al., 2017;
89 Lennartson et al., 2018). Finally, there has been to our knowledge no study of how coarse anthropogenic PM may
90 contribute to the AOD measurements. Coarse anthropogenic PM (distinct from desert dust) is known to be high over
91 East Asia (Chen et al., 2015; Dai et al., 2018).

92 **2 Data and methods**

93 **2.1 Observations**

94 We use observations over China and South Korea from multiple platforms including surface sites, aircraft, and
95 satellites (Table 1 and 2). Surface data (Table 1) include $PM_{2.5}$ from national observation networks in China (Zhai et
96 al., 2019) and South Korea (Jordan et al., 2020), speciated $PM_{2.5}$ at 7 supersites in South Korea during KORUS-AQ
97 (Choi et al., 2019), and ground-based AODs from the AERONET network at 5 sites in North China and 10 sites in
98 South Korea (21 sites during KORUS-AQ). We use total and fine-mode AODs at 500 nm wavelength from the
99 AERONET Version 3; Spectral Deconvolution Algorithm (SDA) Version 4.1 Retrieval Level 2.0 database (Giles et
100 al., 2019; O'Neill et al., 2003). The AERONET AODs at 500 nm are converted to 550 nm using total and fine mode
101 Ångström Exponents at 500 nm for consistency with the satellite AOD data.

102 **Table 1. Surface site observations used in this work (2016)**

Variable	Number of sites
PM _{2.5} in North China ^a	117
PM _{2.5} in South Korea ^b	130
PM _{2.5} composition in South Korea (May-June 2016) ^c	7
AERONET total and fine mode AOD in North China ^d	5
AERONET total and fine mode AOD in South Korea ^d	10-21 ^e

103 ^a Hourly PM_{2.5} from the China National Environmental Monitoring Centre (CNEMC; quotsoft.net/air/) in North
 104 China (115.5-122° E, 34.5-40.5° N), including only sites with more than 90% data coverage in each month of 2016.
 105 Quality control of the CNEMC dataset is described in our previous study (Zhai et al., 2019). The PM_{2.5}
 106 measurements are made at reference RH ≤ 35%.

107 ^b Hourly PM_{2.5} from the AirKorea network (airkorea.or.kr), with the same data selection criteria as for North China.
 108 The PM_{2.5} measurements are made at reference RH ≤ 35%.

109 ^c Major PM_{2.5} components including sulfate, nitrate, ammonium, organic carbon, and black carbon at 7 supersites in
 110 South Korea during KORUS-AQ (May-June 2016; Choi et al., 2019). The mass concentration of organic carbon is
 111 converted to that of organic aerosol with a multiplicative factor of 1.8 based on KORUS-AQ observations (Kim et
 112 al., 2018).

113 ^d AODs are from the AERONET Version 3 Level 2.0 all-points database (aeronet.gsfc.nasa.gov), except that AODs
 114 at the XuZhou site in North China are from the Version 3 Level 1.5 database. AOD at 500 nm (AOD_{500nm}) is
 115 converted to 550 nm (AOD_{550nm}) using Ångström Exponent at 500 nm (AE_{500nm}) following: $AOD_{550nm} =$
 116 $AOD_{500nm} \left(\frac{550}{500}\right)^{-AE_{500nm}}$.

117 ^e AERONET AODs in South Korea are from 10 sites for the full year of 2016 and 21 sites during KORUS-AQ.

118 The KORUS-AQ campaign (Table 2) includes 20 flights over the Korean peninsula and the surrounding ocean from
 119 May 2 to June 10, 2016, with vertical profiling up to 8 km altitude. We use the aircraft observations of remote and in
 120 situ aerosol extinction (scattering + absorption) coefficients, dry aerosol number size distributions, sub-micron non-
 121 refractory aerosol composition, bulk aerosol ionic composition, black carbon (BC), and relative humidity (RH).

122 Geostationary satellite AOD at 550 nm are retrieved by the Yonsei Aerosol Retrieval (YAER) algorithm for the
 123 GOCI (Choi et al., 2016, 2018) and AHI (Lim et al. 2018) instruments, with GOCI covering East China and South
 124 Korea and AHI covering the broad East Asia region. AOD from GOCI and AHI have a 6 km × 6 km spatial
 125 resolution and 1-hour (GOCI) to 2.5-minute (AHI) temporal resolution for 8 hours per day (09:30 to 16:30 local
 126 time). We use the fused AOD product generated from the Yonsei GOCI and AHI AOD retrievals, each using two
 127 different surface reflectance methods (Lim et al., 2021). Fusion of this four-member ensemble is done by the
 128 maximum likelihood estimate (MLE) method, with weighting and averaging based on errors determined by
 129 comparison to AERONET AOD. The fused satellite AOD product is shown by Lim et al. (2021) to have higher
 130 accuracy than its member products in comparison with AERONET data during the KORUS-AQ campaign. We will
 131 refer to it as the ‘GEO satellite AOD’ product in what follows.

132 **Table 2. KORUS-AQ aircraft observations used in this work (May-June 2016).**

Variable	Instrument
Aerosol extinction profile at 532 nm	HSRL ^a
Aerosol scattering coefficient at 550 nm	TSI nephelometers ^b
Aerosol absorption coefficient at 532 nm	PSAPs ^c
Aerosol dry size distribution	TSI LAS ^d
Bulk aerosol ionic composition	SAGA ^e
Sub-micron non-refractory aerosol composition	HR-ToF-AMS ^f
Black carbon concentration	HDSP2 ^g
Relative humidity	DLH ^h

133 ^a NASA Langley airborne High Spectral Resolution Lidar (HSRL) (Hair et al., 2008; Scarino et al., 2014).

134 ^b NASA Langley TSI-3563 nephelometers (Ziemba et al., 2013).

135 ^c Radiance Research 3-wavelength particle soot absorption photometers (PSAPs; Ziemba et al., 2013).

136 ^d In-situ particle size distributions over the 0.1-5.0 μm diameter range from the TSI Laser Aerosol Spectrometer
137 (LAS) Model 3340.

138 ^e University of New Hampshire (UNH) Soluble Acidic Gases and Aerosol (SAGA) instrument (Dibb et al., 2003).
139 The cutoff aerodynamic diameter of the inlet is around 4 μm , corresponding to a geometric particle diameter of 2.5
140 μm (McNaughton et al., 2007; McNaughton et al., 2009).

141 ^f University of Colorado Boulder High-Resolution Time-of-Flight Aerosol Mass Spectrometer (HR-ToF-AMS;
142 DeCarlo et al., 2006; Nault et al., 2018; Guo et al., 2020).

143 ^g NOAA Humidified-Dual-Single-Particle Soot Photometer (HDSP2; Lamb et al., 2018).

144 ^h NASA Diode Laser Hygrometer (DLH; Podolske et al., 2003).

145 **2.2 GEOS-Chem simulation**

146 We use GEOS-Chem version 12.7.1 (DOI: 10.5281/zenodo.3676008) in a nested-grid simulation at a horizontal
147 resolution of $0.5^\circ \times 0.625^\circ$ over East Asia (100-145 $^\circ\text{E}$, 20-50 $^\circ\text{N}$). GEOS-Chem simulates detailed tropospheric
148 oxidant-aerosol chemistry and is driven here by GEOS-FP assimilated meteorological data from the NASA Global
149 Modeling and Assimilation Office (GMAO). Boundary layer mixing uses the non-local scheme implemented by Lin
150 and McElroy (2010). Dry deposition of gases and particles follows a standard resistance-in-series scheme (Zhang et
151 al., 2001; Fairlie et al., 2007; Fisher et al., 2011; Jaeglé et al., 2018). Wet deposition of gases and particles includes
152 contributions from rainout, washout, and scavenging in convective updrafts (Liu et al., 2001; Amos et al., 2012; Q.
153 Wang et al., 2011; Q. Wang et al., 2014) with recent updates by Luo et al. (2019, 2020). We use pre-archived initial

154 conditions from Zhai et al. (2021) and run the model from December 1, 2015 to December 31, 2016. The first month
155 is used for spin-up and the year 2016 is used for analysis.

156 GEOS-Chem has been used extensively to simulate PM_{2.5} and its composition in East Asia (Geng et al., 2017; Li et
157 al., 2016; Choi et al., 2019; Jeong et al., 2008; Park et al., 2021; Zhai et al., 2021). Here we use the bulk
158 representation of aerosols including sulfate (Park et al., 2004; Alexander et al., 2009), nitrate (Jaeglé et al., 2018),
159 primary and secondary organics (Pai et al., 2020), BC (Q. Wang et al., 2014), natural dust in four advected size
160 ranges (Fairlie et al., 2007), anthropogenic fine dust (Philip et al., 2017), and sea salt in two size ranges (Jaeglé et
161 al., 2011). Heterogeneous sulfate formation on aqueous aerosols is represented by a simplified parameterization
162 scheme (Y. Wang et al., 2014), where the SO₂ uptake coefficient (γ) linearly increases from 1×10^{-5} at RH \leq 50% to
163 2×10^{-5} at RH = 100%. The thermodynamic equilibrium of sulfate-nitrate-ammonium (SNA) aerosols with the gas
164 phase is computed with ISORROPIA II (Fountoukis and Nenes, 2007; Pye et al., 2009) assuming an aqueous
165 aerosol. We include reactive uptake on dust of acid gases (HNO₃, SO₂, and H₂SO₄), limited by consumption of dust
166 alkalinity (Fairlie et al., 2010). The alkalinity of emitted dust is estimated by assuming 7.1% Ca²⁺ and 1.1% Mg²⁺ as
167 alkaline cations by dust mass (Shah et al., 2020).

168 Monthly anthropogenic emissions are from the Multi-resolution Emission Inventory in 2016 for China (MEIC;
169 Zheng et al., 2018; <http://meicmodel.org>) and from the KORUSv5 emission inventory at base year 2015 (Woo et al.,
170 2020; http://aisl.konkuk.ac.kr/#/emission_data/korus-aq_emissions) for other Asian countries and shipping
171 emissions. MEIC over China applies weekly and diurnal scaling factors for all anthropogenic emissions (Zheng et
172 al., 2018). The KORUSv5 agricultural NH₃ emissions apply the diurnal scaling factors from MEIC. Natural
173 emissions include NO_x from lightning (Murray et al., 2012) and soil (Hudman et al., 2012), MEGANv2 biogenic
174 volatile organic compounds (VOCs) (Guenther et al., 2012), dust (Meng et al., 2020), and sea salt (Jaeglé et al.,
175 2011). Open fire emissions are from the Global Fire Emissions Database version 4 (GFED4; van der Werf et al.,
176 2017).

177 **2.3 AOD simulation**

178 AOD in GEOS-Chem is diagnosed by integrating vertically the aerosol scattering and absorption coefficients
179 obtained with a standard Mie calculation applied to assumed size distributions, hygroscopicity, refractive indices,
180 and densities for individual aerosol components, and summing over all components (Martin et al., 2003). Optical
181 properties are listed in Table 3. Sulfate, nitrate, and ammonium share the same optical properties and are lumped as
182 an SNA aerosol component for the purpose of optical calculations. All aerosol components except dust are assumed
183 to follow log-normal size distributions. Dust includes 7 size bins (centered at radii of 0.15, 0.25, 0.4, 0.8, 1.5, 2.5,
184 and 4.0 μm) for optical calculations, with the smallest four bins partitioned by mass from the first advected dust bin
185 ($< 2.5 \mu\text{m}$ in geometric diameter) following L. Zhang et al. (2013). Dust particles follow a gamma size distribution
186 within their optical size bins (Curci, 2012). The BC absorption enhancement from coating is as given by X. Wang et
187 al. (2014).

188 Our initial simulations indicated that aerosol extinction coefficients from the standard GEOS-Chem version 12.7.1
 189 underestimated in situ measured extinction coefficients during KORUS-AQ by 20% on average (Figure S1). We
 190 traced this problem to bias in the assumed size distributions for SNA and organic aerosol, as shown in Section 3.
 191 Therefore, we re-computed the diagnostic AOD using updated log-normal size distributions for SNA and organic
 192 aerosol with number median radius $R_{N,med} = 0.11 \mu\text{m}$ and geometric standard deviation $\sigma = 1.4$ based on KORUS-
 193 AQ observations, instead of $R_{N,med} = 0.058 \mu\text{m}$ and $\sigma = 1.6$ in the standard model version 12.7.1, which is derived
 194 from IMPROVE network measurements of aerosol mass scattering efficiency over North America (Latimer and
 195 Martin, 2019).

196 **Table 3. Aerosol optical properties ^a.**

Aerosol component	$R_{N,med}$, μm	σ	Hygroscopicity ^b	Refractive index	ρ , g cm^{-3}
SNA ^c	0.11	1.4	$\kappa = 0.61$	$1.53 - 6.0 \times 10^{-3}i$	1.7
Organic ^c	0.11	1.4	$\kappa = 0.1$	$1.53 - 6.0 \times 10^{-3}i$	1.3
BC	0.020	1.6	GADS	$1.75 - 4.4 \times 10^{-3}i$	1.8
Sea salt (fine)	0.085	1.5	GADS	$1.5 - 1.0 \times 10^{-3}i$	2.2
Sea salt (coarse)	0.40	1.8	GADS	$1.5 - 1.0 \times 10^{-3}i$	2.2
Dust	7 size bins	NA	$\kappa = 0$ ^d	$1.558 - 1.4 \times 10^{-3}i$	2.5-2.65 ^e

197 ^a Aerosol optical properties used in this work for computing aerosol scattering and absorption coefficients. Values
 198 are from the standard GEOS-Chem model version 12.7.1, except for the size distributions of SNA and organic
 199 aerosol which are based on KORUS-AQ observations (see text). All aerosol components except dust have log-
 200 normal dry size distributions where $R_{N,med}$ is the number median radius and σ is the geometric standard deviation.
 201 Refractive indices are for 550 nm wavelength. ρ is the dry aerosol mass density.

202 ^b Hygroscopic growth for SNA and organic aerosol as a function of relative humidity (RH, %) is computed from κ -
 203 Kohler theory as a diameter growth factor $GF = (1 + \kappa * RH/(100-RH))^{1/3}$ (Latimer and Martin, 2019). Hygroscopic
 204 growth factors for other aerosol components are from the Global Aerosol Data Set (GADS) as tabulated in Chin et
 205 al. (2002) and Martin et al. (2003).

206 ^c $R_{N,med}$ and σ are fit to KORUS-AQ observations as described in the text. Standard GEOS-Chem v12.7.1 assumes
 207 $R_{N,med} = 0.058 \mu\text{m}$, $\sigma = 1.6$ (Latimer and Martin, 2019).

208 ^d Hygroscopic growth of dust particles is assumed negligible.

209 ^e Sub-micron dust particles have a density of 2.5 g cm^{-3} while coarse mode dust particles have a density of 2.65 g
 210 cm^{-3} . Dust size distribution is described in the text.

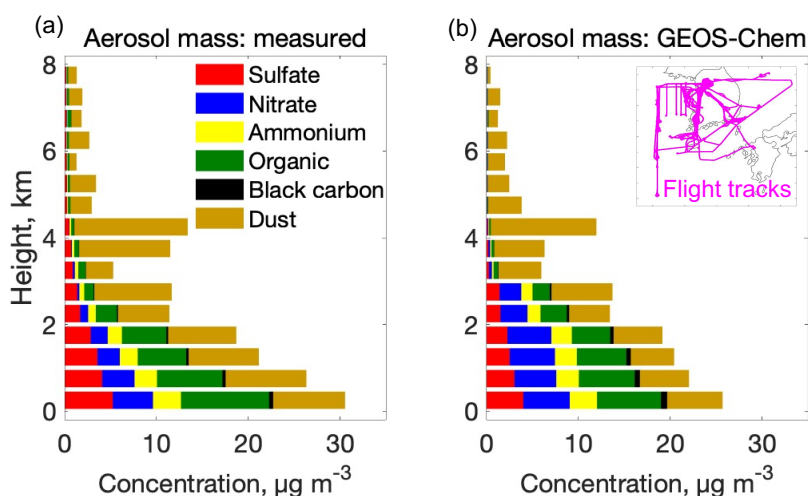
211 3 Aerosol concentrations and optical properties during KORUS-AQ

212 Here we use the KORUS-AQ aircraft observations and their simulation with GEOS-Chem to better understand the
 213 vertical distributions of different aerosol components contributing to AOD over South Korea. We begin with the
 214 mean vertical profile of aerosol mass and go on to examine the aerosol optical properties. This provides the basis for
 215 analyzing the observed vertical profile of aerosol extinction, its simulation by GEOS-Chem, and the consistency
 216 with GEO satellite and AERONET AOD measurements over South Korea during the KORUS-AQ period.

217 3.1 Vertical profile of aerosol mass

218 Figure 1 shows the mean vertical profiles of aerosol mass observed during KORUS-AQ and their simulation by
 219 GEOS-Chem. Here and elsewhere, the model is sampled along the flight tracks and at the flight times. The observed
 220 vertical distribution of aerosol mass concentrations (Figure 1a) shows that 58% of column aerosol mass is below 2
 221 km altitude, which we define as the average planetary boundary layer (PBL) during KORUS-AQ, and 34% is at 2-5
 222 km altitude, which we define as the lower free troposphere (FT). The model has a similar vertical distribution
 223 (Figure 1b), with 57% of aerosol mass in the PBL and 36% in the lower FT. SNA, organic, and dust each contribute
 224 about a third of aerosol mass in the PBL while dust dominates in the lower FT both in the observations and in the
 225 model. The enhanced dust in the lower FT is driven by a few dust events, which the model reproduces (Figure S2).
 226 Black carbon and sea salt (not shown) make only minor contributions to aerosol mass. The model underestimates
 227 sulfate by 28% in the PBL, which leads to a 20% overestimate of nitrate, with canceling effect on the SNA mass
 228 simulation.

229 The GEOS-Chem simulation of organic aerosol in this work uses the simple scheme of Pai et al. (2020) and
 230 underestimates aircraft observations by 16% in the PBL. Over 90% of GEOS-Chem organic aerosol is secondary,
 231 consistent with observations (Figure S4; Nault et al., 2018; Pai et al., 2020). GEOS-Chem simulation of the
 232 KORUS-AQ aerosol component profiles for different meteorological regimes is presented in Park et al. (2021).



233
 234 **Figure 1. Vertical profiles of aerosol mass during KORUS-AQ.** Panel (a) shows the mean vertical distributions of
 235 observed mass concentrations of major aerosol components at ambient temperature and pressure. Panel (b) is the same as
 236 (a) but from the GEOS-Chem model sampled along the flight tracks (inset). We derive dust concentration from SAGA
 237 Ca²⁺ and Na⁺ following Shah et al. (2020) by assuming that non-sea salt Ca²⁺ accounts for 7.1% of dust mass: [dust] =
 238 $([Ca^{2+}] - 0.0439 [Na^+]/2) / 0.071$ where the brackets denote mass concentration. Modeled dust is shown for particles with
 239 geometric diameter < 2.5 µm, to be consistent with SAGA measurements (Table 2 footnote e). Measured sulfate, nitrate,
 240 ammonium, and organic aerosol concentrations are from the AMS instrument (values from the SAGA instrument are
 241 shown in Figure S4). All data are averaged over 500-m vertical bins. Here and elsewhere, we excluded pollution plumes
 242 diagnosed by either NO₂ or SO₂ > 10 ppbv (3.4% of all the data).

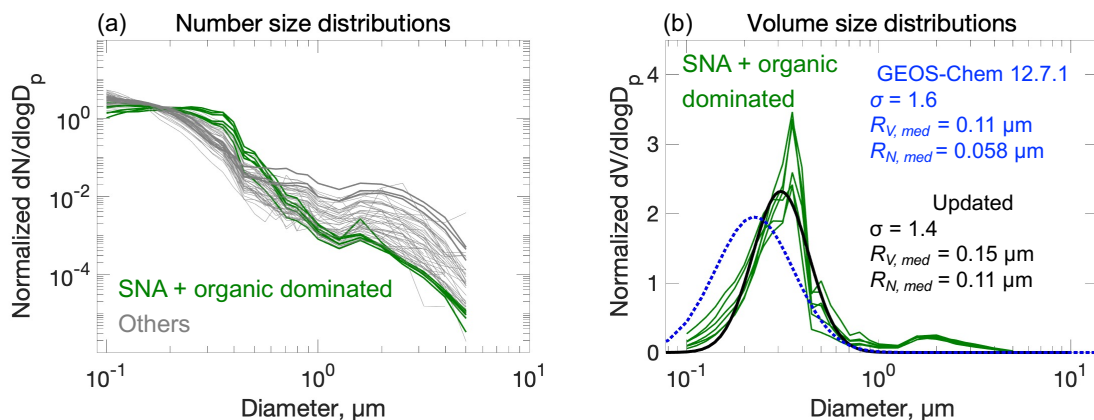
243 **3.2 Aerosol size distributions**

244 Figure 2a shows the normalized dry aerosol number size distributions on each of the 20 flights and in 3 altitude
 245 bands: < 1.5 km, 3-5 km, and 6-7 km (60 lines). The spread in the size distributions above 1 μm in diameter reflects
 246 dust influence. We select measurements below 1.5 km altitude when SNA + organic aerosol mass concentrations are
 247 more than 4 times that of dust as defining the SNA + organic aerosol size distributions (green lines in Figure 2a).
 248 Conditions dominated by SNA + organic aerosols define the lower envelopes of the ensemble of size distributions at
 249 diameter > 1 μm . SNA and organics were observed to have similar size distributions during KORUS-AQ (Kim et
 250 al., 2018).

251 Figure 2b converts the SNA + organic dominated number size distributions to volume size distributions. The
 252 observed SNA + organic dominated aerosol size distribution is shifted toward larger sizes relative to the standard
 253 GEOS-Chem. The secondary maximum in the coarse mode could be due to dust. We fitted the observed SNA +
 254 organic aerosol size distributions to a lognormal distribution with volume median radius $R_{V,med} = 0.15 \mu\text{m}$ and
 255 geometric standard deviation $\sigma = 1.4$. The number median radius is derived from the volume median radius
 256 following Seinfeld and Pandis (2016):

257
$$\ln R_{N,med} = \ln R_{V,med} - 3\ln^2\sigma \tag{1}$$

258 which yields $R_{N,med} = 0.11 \mu\text{m}$. In comparison, the standard GEOS-Chem size distribution from Latimer and Martin
 259 (2019) has $R_{N,med} = 0.058 \mu\text{m}$ and $\sigma = 1.6$. We adopt the observed log-normal size distribution parameters in what
 260 follows (Table 3).



261
 262 **Figure 2. Aerosol dry size distributions measured in the KORUS-AQ aircraft campaign. Panel (a) shows mean**
 263 **normalized number size distributions measured on each of the 20 flights and for 3 altitude bins: < 1.5 km, 3-5 km, and 6-7**
 264 **km (60 lines total). The SNA + organic dominated size distribution profiles are highlighted in color. Panel (b) shows**
 265 **normalized volume size distributions for conditions dominated by SNA + organic aerosols (green lines), along with a least-**
 266 **square fit to a lognormal distribution (black line), and the standard GEOS-Chem v12.7.1 size distribution from Latimer**
 267 **and Martin (2019) (blue dashed line). Normalization imposes an arbitrary value of unit area below each line. Lognormal**

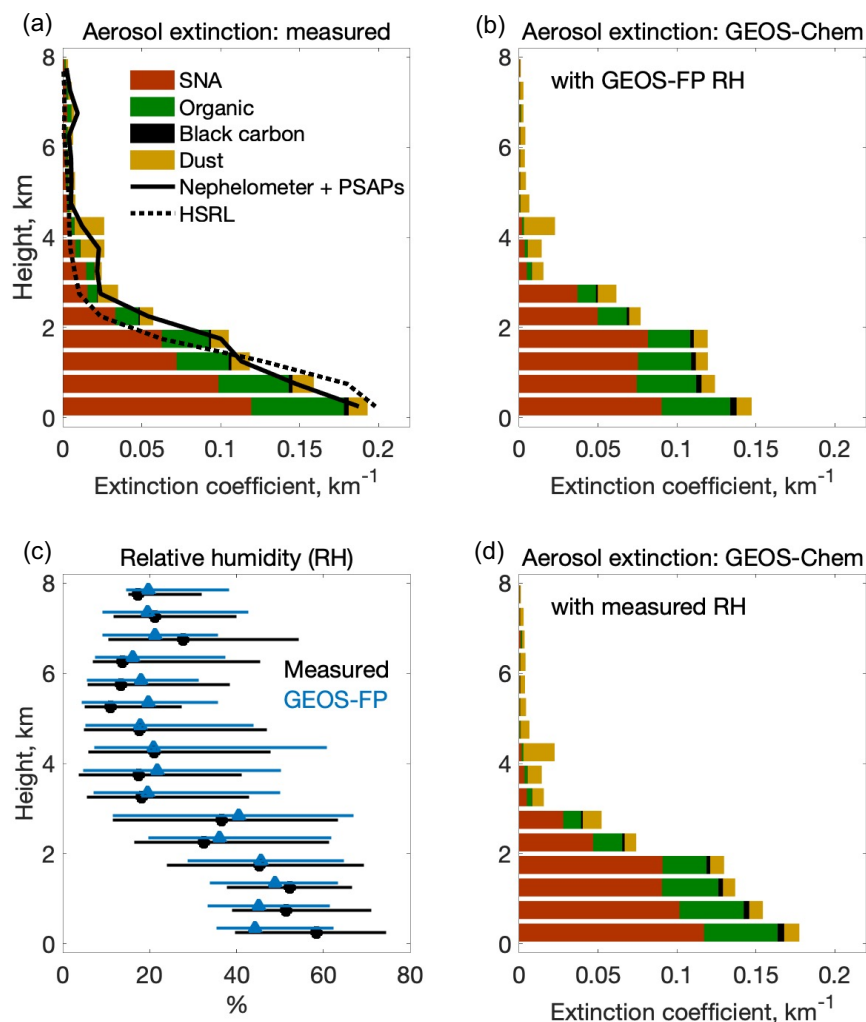
268 distribution parameters are inset in panel (b) including volume median radius ($R_{V,med}$), number median radius ($R_{N,med}$),
269 and geometric standard deviation (σ).

270 3.3 Aerosol extinction and relation to AOD

271 Figure 3 shows the vertical profiles of ambient aerosol extinction coefficients and RH during KORUS-AQ. Vertical
272 profiles of aerosol extinction were measured on the aircraft both remotely with the HSRL instrument (above and
273 below the aircraft) and in situ with TSI-3563 nephelometers (for scattering) and PSAPs (for absorption). The two
274 agree well, as shown in Figure 3a. They indicate that 76-90% of column aerosol extinction is in the PBL at 0-2 km
275 altitude and 9-19% is in the lower FT at 2-5 km. Both measurements show that aerosol extinction is much more
276 strongly weighted to the PBL than aerosol mass (Figure 1).

277 Also shown in Figure 3a are the contributions of individual aerosol components to the extinction profile, as
278 computed from the GEOS-Chem optical properties (Table 3) applied to the observed mass concentrations. The sum
279 shows a good match to the measured extinction coefficient profiles. The much larger contribution of the PBL to
280 column aerosol extinction than to column mass is because aerosol mass in the lower FT is mainly composed of dust,
281 whose mass extinction efficiency is much smaller than SNA and organics due to its coarse size and lack of
282 hygroscopic growth (Figure S5). The mean AOD inferred from the aircraft data is 0.36 and is contributed 59% by
283 SNA, 27% by organic aerosol, 12% by dust, and 2% by BC. It is consistent with the mean AODs measured at
284 AERONET stations in South Korea during KORUS-AQ (Figure S6).

285 Figure 3b shows the GEOS-Chem simulation of aerosol extinction profiles for comparison to the observations in
286 Figure 3a. The model underestimates extinction coefficients by 20% below 1 km altitude, leading to a 10%
287 underestimate of aircraft inferred AOD, although there is no such underestimate in aerosol mass. This is caused by a
288 negative RH bias in the GEOS-FP meteorological data used to drive GEOS-Chem, particularly at high RH
289 conditions (Figure 3c) and is corrected if we apply the observed RH rather than the GEOS-FP RH to the GEOS-
290 Chem aerosol mass concentrations (Figure 3d).



291
 292 **Figure 3. Vertical profiles of aerosol extinction coefficients and relative humidity (RH) during KORUS-AQ. Panel (a)**
 293 **shows the mean observed vertical distributions of 550 nm extinction coefficients measured in situ (nephelometer + PSAPs;**
 294 **at ambient RH) and remotely (HSRL), along with an independent calculation (colored horizontal bars) from the**
 295 **measured mass concentrations of major aerosol components, measured RH, and GEOS-Chem optical properties as given**
 296 **in Table 3. Panel (b) shows the mean aerosol extinction profile in GEOS-Chem and the contributions from the different**
 297 **model components. Panel (c) is the median vertical profile of RH (horizontal bars are 25-75th percentiles) from aircraft**
 298 **measurements and the GEOS-FP assimilated meteorological data used to drive GEOS-Chem. Panel (d) is the same as (b)**
 299 **but calculated using measured RH.**

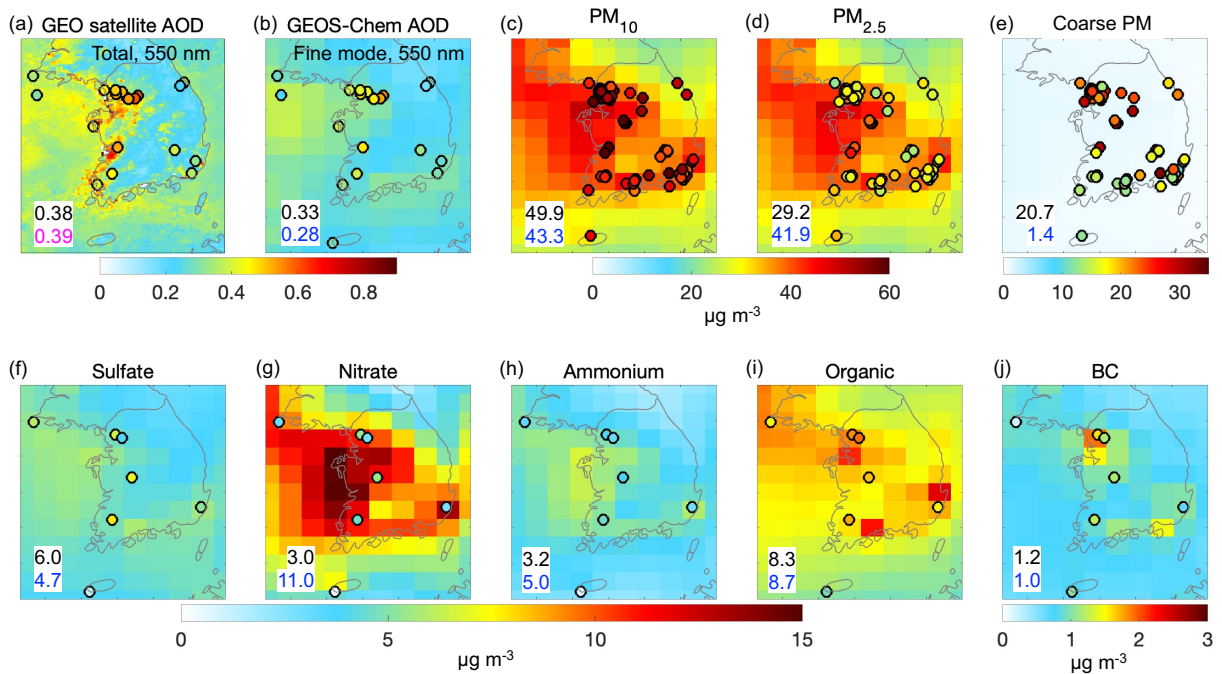
300 4 AOD and surface particulate matter over South Korea during KORUS-AQ

301 Our analysis of Section 3 used the KORUS-AQ aircraft data together with GEOS-Chem to attribute AOD over
 302 South Korea to individual aerosol components and altitudes. We now take the next step of evaluating the capability
 303 of GEOS-Chem to independently simulate observed AODs and surface particulate matter concentrations.

304 Figure 4a shows the spatial distribution of the fused geostationary satellite (GOCI/AHI) AOD (GEO satellite AOD)
305 during the KORUS-AQ period with AERONET total AOD added as circles. The GEO satellite AOD shows high
306 values (0.5-0.6) along the west coast of South Korea, significantly correlated with AERONET total AOD with a
307 spatial correlation coefficient (R) of 0.7. GEO satellite AOD is biased low at sites in the Seoul Metropolitan Area
308 (SMA) and is biased high on the Yellow Sea islands, resulting in an overall -10% bias. The low biases in the SMA
309 could be due to high-concentration aerosol pixels mis-identified as clouds and/or possible issues with the aerosol
310 type assumption in the aerosol retrieval, while the high biases on the Yellow Sea islands could result from
311 uncertainties in the assumption of ocean surface reflectance, as has been discussed by Choi et al. (2016, 2018) and
312 Lim et al. (2018, 2021). Sampling the AODs at or near the seven PM_{2.5} supersites operating during KORUS-AQ
313 shows no significant bias (inset values in Figure 4a).

314 Figure 4b-e shows the spatial distributions of GEOS-Chem AOD, surface PM₁₀ (particulate matter with aerodynamic
315 diameter less than 10 μm), surface PM_{2.5}, and surface coarse PM (PM₁₀ minus PM_{2.5}; particulate matter with
316 aerodynamic diameter less than 10 μm and larger than 2.5 μm), with surface observations shown as circles and
317 median values at the measurement sites inset. GEOS-Chem reproduces the satellite AOD enhancements along the
318 west coast of South Korea but the values are lower than observed, which we attribute to unaccounted coarse PM and
319 negative RH bias as discussed below. Comparison of AERONET total and fine mode AOD shows a 13%
320 contribution of coarse particles to total AOD. Comparison of GEOS-Chem to the fine-mode AERONET AOD, as
321 shown in Figure 4b, finds a 15% underestimate that could be attributed to the low-RH bias (Figure 3c). Concurrent
322 measurements of PM₁₀ and PM_{2.5} at AirKorea sites show that coarse PM (median 21 $\mu\text{g m}^{-3}$) accounts for 41% of
323 total PM₁₀ (50 $\mu\text{g m}^{-3}$), while coarse PM in GEOS-Chem is much lower (1.4 $\mu\text{g m}^{-3}$; Figure 4e). Therefore, about
324 half of the GEOS-Chem underestimate of total AOD can be attributed to missing coarse PM, with the other half
325 comes from negative RH bias. Coarse PM has a concentration larger than 10 $\mu\text{g m}^{-3}$ across South Korea, with higher
326 concentration in the SMA ($\sim 30 \mu\text{g m}^{-3}$) than in rural areas ($\sim 15 \mu\text{g m}^{-3}$), implying an origin from both
327 anthropogenic and natural sources (Figure 4e).

328 GEOS-Chem overestimates surface PM_{2.5} by 43% over South Korea (Figure 4d), in contrast to the simulation of
329 AERONET fine mode AOD (Figure 4b). Figure 4f-j shows the spatial distributions of major PM_{2.5} components in
330 GEOS-Chem (background) and measurements (filled circles). GEOS-Chem is not significantly biased relative to the
331 observations for organic aerosol and BC, and underestimates sulfate by 22%. We find that the model bias for PM_{2.5}
332 is largely driven by nitrate, which is overestimated by a factor of 3 and leads to a 56% overestimate of ammonium.
333 By contrast, comparison to the KORUS-AQ data below 1-km altitude showed only a 20% overestimate of nitrate
334 (Figure 1). This is because the model bias is mainly driven by nighttime conditions, as shown in Figure 5. The cause
335 of this large model bias is analyzed by K. R. Travis et al. (manuscript in preparation) and is attributed to nighttime
336 nitrate chemistry and deposition in the stratified boundary layer.



Ground measurements (filled circles) Geostationary satellite (background in panel a) GEOS-Chem (background in panels b-j)

337

338

339

340

341

342

343

344

345

346

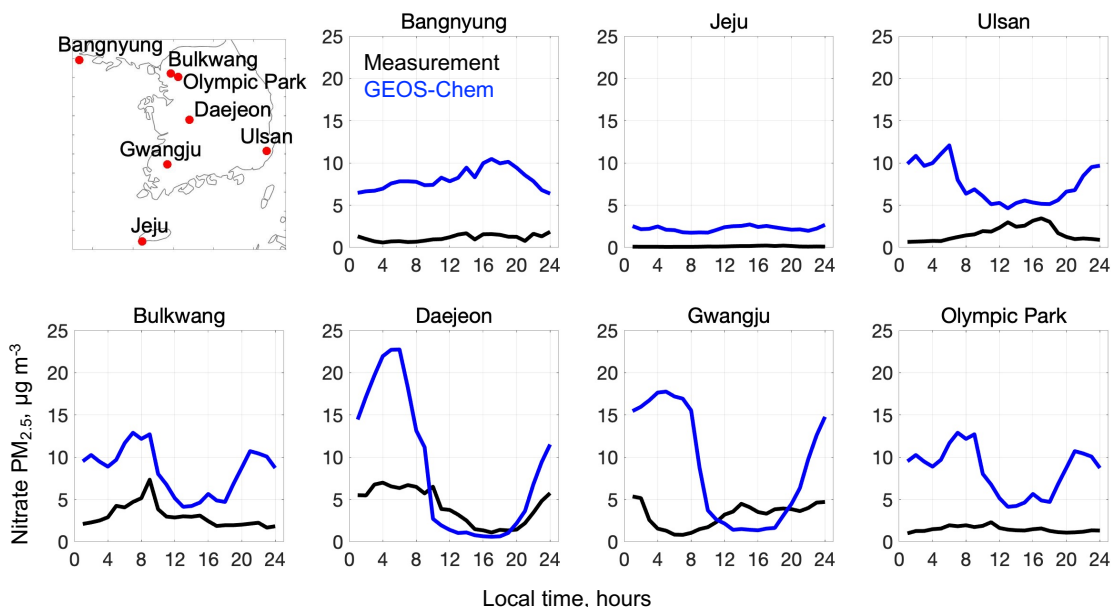
347

348

349

350

Figure 4. Spatial distributions of AOD and surface PM₁₀, PM_{2.5}, coarse PM (PM₁₀ minus PM_{2.5}), and major PM_{2.5} components over South Korea averaged during KORUS-AQ (May 9 - June 10, 2016). Panel (a) shows the fused geostationary (GEO) 550 nm AOD from the GOCI and AHI satellites (background) and AERONET 550 nm total AOD (filled circles). Panel (b) shows GEOS-Chem 550 nm AOD sampled at hourly GEO satellite AOD (GEOS-Chem clear-sky AOD; background) and AERONET 550 nm fine mode AOD (filled circles). Panel (c) shows surface PM₁₀ modelled by GEOS-Chem (background) and measured at ground sites (filled circles). Panels (d-j) are the same as panel (c) but respectively for PM_{2.5}, coarse PM (PM₁₀ minus PM_{2.5}), and sulfate, nitrate, ammonium, organic, and BC PM_{2.5} components. Values inset are median values from ground-based measurements (black) and sampled from GEO satellite (magenta) and GEOS-Chem (blue). Measured PM₁₀, PM_{2.5}, and coarse PM in panels (c-e) are shown for a random selection of 50% of AirKorea sites to visualize spatial distribution, and inset values are for the seven supersites where PM_{2.5} composition was measured. Median AOD values inset are sampled at or near the seven supersites to avoid biasing by the large number of sites in the Seoul Metropolitan Area. Modelled total PM_{2.5} concentrations are calculated at 35% RH (Table 3). Modelled PM₁₀ is the sum of PM_{2.5}, coarse dust, and coarse sea salt.



351
 352 **Figure 5. Median diurnal variations of PM_{2.5} nitrate concentrations at the seven supersites (top left panel) operated in**
 353 **South Korea during KORUS-AQ (May 9 - June 10, 2016). Values are medians binned by hour. GEOS-Chem model**
 354 **values are sampled to coincide with the measurements.**

355 5 AOD and its relationship to PM_{2.5} over East Asia

356 We build on our analysis of the KORUS-AQ period for a broader interpretation of the distribution of AOD over
 357 Korea and China and its relationship to surface PM_{2.5}, acknowledging that the conditions sampled in KORUS-AQ
 358 may not be representative of other seasons or of China. Figure 6 shows the spatial distributions of 2016 annual and
 359 seasonal mean geostationary (GEO) satellite AODs, the corresponding GEOS-Chem clear-sky AODs, and GEOS-
 360 Chem surface PM_{2.5}. The Figure gives normalized mean biases (*NMBs*) relative to ground-based measurements from
 361 AERONET and from the PM_{2.5} surface networks (shown as circles).

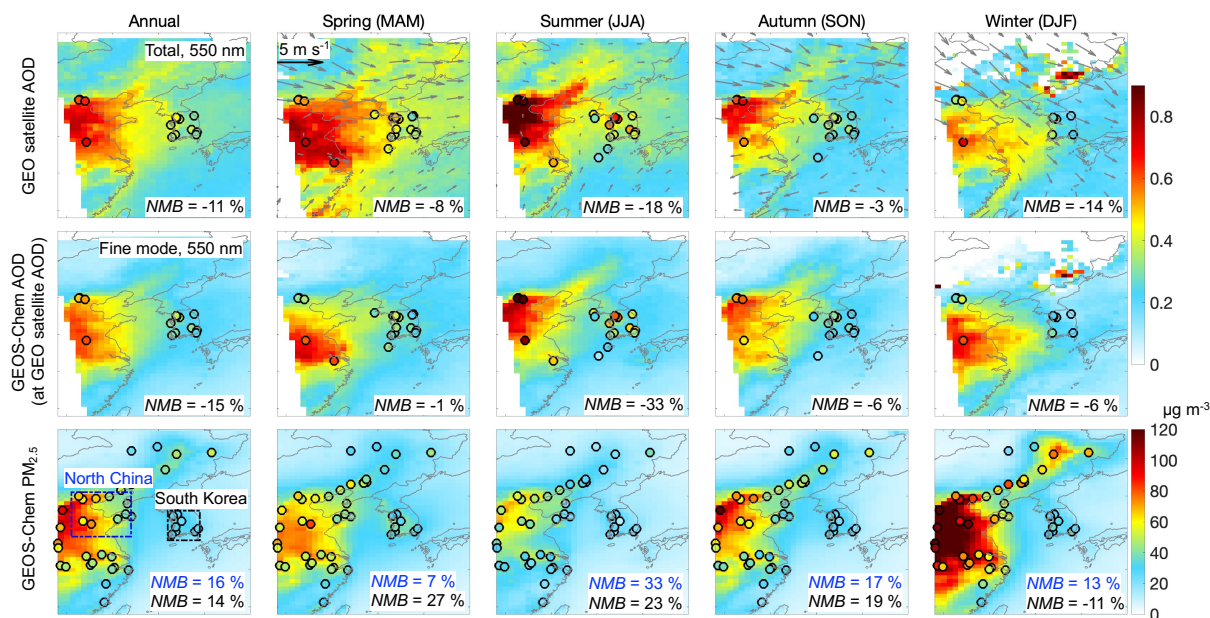
362 On an annual mean basis, AOD over North China (~ 0.5-0.6) is about 50% larger than over South Korea (~ 0.3-0.4).
 363 AOD over South Korea shows higher values (> 0.4) in the Seoul Metropolitan Area, consistent with that during the
 364 KORUS-AQ period (Figure 4a). Transport from the Asian continent is strongest in spring when the frequency of
 365 cold front passages is highest (Liu et al., 2003). AERONET total AOD in spring (0.4-0.6) is twice as large as fine-
 366 mode AOD (0.2-0.3), reflecting a large contribution of dust. In seasons other than spring, 80-90% of AERONET
 367 total AOD is contributed by the fine mode. There is large seasonality in AODs over North China, and weaker
 368 seasonality over South Korea, which will be discussed below.

369 The GEOS-Chem clear-sky AODs show the same spatial and seasonal patterns as GEO satellite AODs but tend to
 370 be low in spring and summer. Comparison of the model to AERONET AODs confirms this bias and shows better
 371 agreement with fine-mode AOD in spring (*NMB* of -1%), implying an underestimate of coarse dust that is consistent
 372 with our comparisons to the AirKorea PM₁₀ network data (Figure 4e). Comparison of clear-sky and all-sky AODs in

373 GEOS-Chem shows no significant difference on an annual and seasonal mean basis, except for winter (Figure S7).
 374 Winter has larger all-sky AOD than clear-sky AOD and the lowest rate of successful satellite retrievals (Figure S7),
 375 which may be due in part to misclassification of heavy wintertime $PM_{2.5}$ pollution as clouds (Zhang et al., 2020).

376 The spatial distributions of $PM_{2.5}$ in GEOS-Chem in different seasons match closely the observations (Figure 6,
 377 bottom row). We see also a close coincidence between the spatial distributions of $PM_{2.5}$ and AODs, both in the
 378 observations and the model. On an annual mean basis, GEOS-Chem overestimates $PM_{2.5}$ by 16% in North China
 379 and by 14% in South Korea, even though it underestimates AERONET fine mode AODs by 15%. The overestimate
 380 of $PM_{2.5}$ in South Korea is worst in spring (27%), consistent with KORUS-AQ results which we previously
 381 attributed to excessive nighttime nitrate build-up in the model. Over North China, the overestimate of $PM_{2.5}$ is worst
 382 in summer (33%), consistent with the nitrate overestimate in summer shown in our previous study (Zhai et al.,
 383 2021), which could also be due to model overestimate of nighttime nitrate (Miao et al., 2020).

384

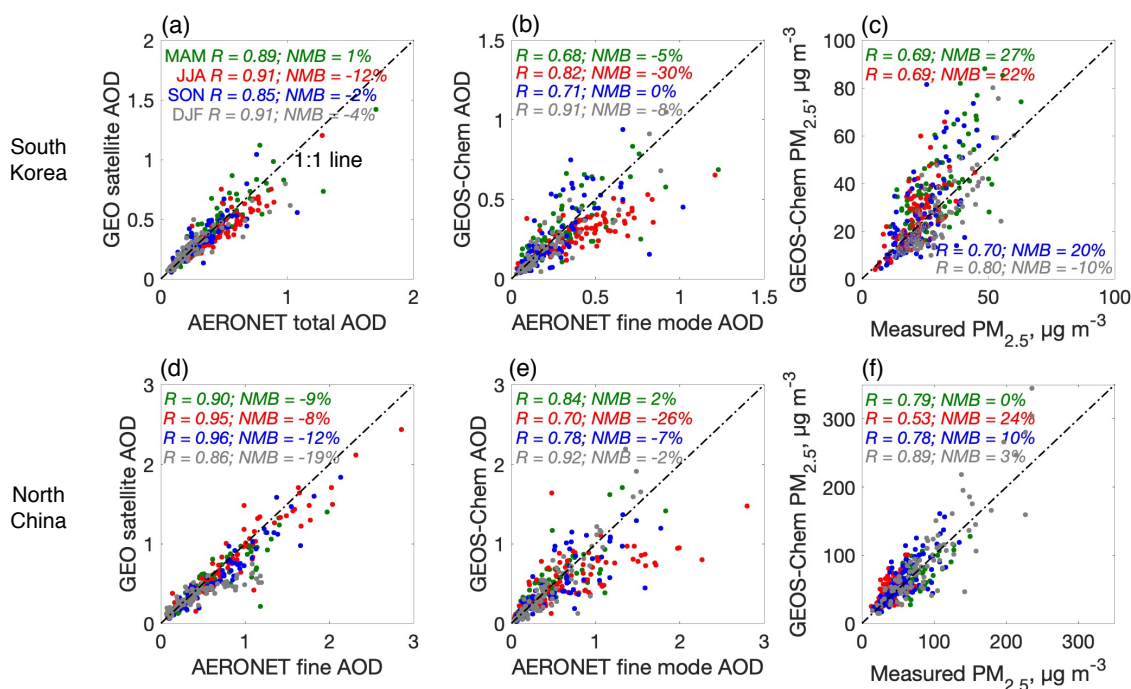


385
 386 **Figure 6. Spatial distributions of 2016 annual and seasonal mean AOD (550 nm) and surface $PM_{2.5}$. The top row shows**
 387 **the observed GOCI/AHI geostationary satellite AOD (GEO satellite AOD) on the GEOS-Chem $0.5^\circ \times 0.625^\circ$ grid with**
 388 **superimposed 925 hPa GEOS-FP wind fields and AERONET total AODs (circles). The middle row shows clear-sky**
 389 **GEOS-Chem AOD, with AERONET fine mode AOD added as circles. The bottom row shows GEOS-Chem surface $PM_{2.5}$**
 390 **(background) with surface network measurements (circles). AERONET AODs are shown only when more than 10**
 391 **months of data are available for the annual mean and all 3 months data are available for each season. The $PM_{2.5}$**
 392 **observations shown are for a random selection of 7% of network sites for visual clarity. GEOS-Chem $PM_{2.5}$ is calculated**

393 at 35% RH (Table 3). Normalized mean biases (*NMBs*) inset are for the comparisons of GEO satellite and GEOS-Chem
 394 values to the corresponding ground measurements.

395

396 Figure 7 shows daily correlations of the regional average series between AERONET total AOD and GEO satellite
 397 AOD, between AERONET fine mode AOD and GEOS-Chem AOD, as well as between measured PM_{2.5} and GEOS-
 398 Chem PM_{2.5}. Correlations in Figure 7 are all statistically significant with correlation coefficients (*R*) ranging from
 399 around 0.7 to more than 0.9 and normalized mean biases (*NMB*) within $\pm 30\%$. The correlations of these three pairs
 400 are similar over South Korea and North China, except that GEOS-Chem overestimates springtime PM_{2.5} in South
 401 Korea but not over North China, possibly due to a model overestimate of the long-range transport of PM_{2.5} from
 402 China to South Korea in spring.



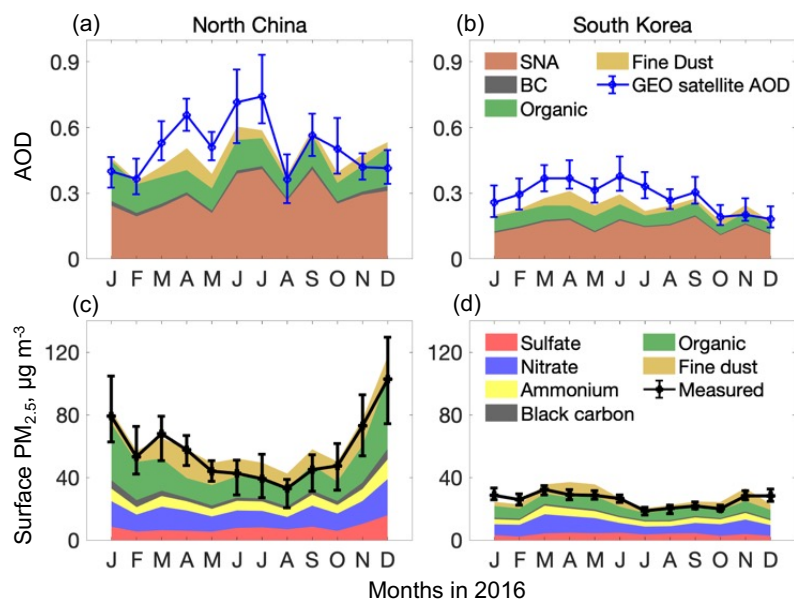
403
 404 **Figure 7. Scatter plots of regional mean daily (a and d) GEO satellite AOD vs. AERONET total AOD, (b and e) GEOS-**
 405 **Chem AOD vs. AERONET fine-model AOD, and (c and f) GEOS-Chem PM_{2.5} vs. measured PM_{2.5} over South Korea (a-c)**
 406 **and North China (d-f). Different colors represent different seasons. Values inset are correlation coefficients (*R*) and**
 407 **normalized mean biases (*NMB*) between surface measurements and GEO satellite or GEOS-Chem values.**

408

409 Figure 8 compares the seasonalities of AOD and PM_{2.5} over the North China and South Korea regions. The GEO
 410 satellite AOD over North China peaks in July and is minimum in winter. Most of AOD is attributed by GEOS-Chem
 411 to SNA aerosol, same as in South Korea. AOD over South Korea also has a summer maximum and winter minimum
 412 but with weaker amplitude than over North China. The GEOS-Chem AOD is $\sim 20\%$ biased low in summer and this

413 is largely due to a low RH bias (Figure S8), as seen previously in the KORUS-AQ comparisons but amplified by the
 414 high RH in summer that drives hygroscopic growth (Latimer and Martin, 2019).

415 Surface $PM_{2.5}$ in the observations over North China and South Korea shows opposite seasonality to AOD, with
 416 minimum values in summer and maximum values in winter-spring. GEOS-Chem reproduces the strong seasonality
 417 of $PM_{2.5}$ in North China and the much weaker seasonality in South Korea. The high $PM_{2.5}$ values over North China
 418 in winter in the model are mostly driven by organic aerosol, reflecting the large residential coal burning source
 419 (Figure S9; Zheng et al., 2018). In South Korea, by contrast, household energy is mainly from natural gas and
 420 electricity (Lee et al., 2020; Woo et al., 2020). GEOS-FP daytime PBL height also shows a stronger seasonality over
 421 North China than over South Korea (Figure S8), generally consistent with the CALIPSO daytime PBL height (Su et
 422 al., 2018). Previous studies have shown opposite seasonality between MODIS AOD and surface $PM_{2.5}$ over North
 423 China and attributed this to the seasonality in PBL height and RH (Qu et al., 2016; Xu et al., 2019). The mean
 424 $PM_{2.5}$ /AOD ratio over North China in winter ($236 \mu\text{g m}^{-3}$) is 8 times that in summer ($29 \mu\text{g m}^{-3}$), with autumn ($94 \mu\text{g m}^{-3}$)
 425 m^{-3}) and spring ($89 \mu\text{g m}^{-3}$) in between, while over South Korea, the $PM_{2.5}$ /AOD ratio in winter ($62 \mu\text{g m}^{-3}$) is only
 426 70% larger than in summer ($36 \mu\text{g m}^{-3}$).



427
 428 **Figure 8. Seasonality of AOD and $PM_{2.5}$ over North China and South Korea, and contributions from individual aerosol**
 429 **components. Lines show regional medians (error bars: 25th and 75th percentiles) for the ensemble of monthly averaged**
 430 **observations in the regions (Figure 6) in 2016. GEOS-Chem values are shown as stacked contours for individual**
 431 **components and are sampled in the same way as the observations.**

432 6 Conclusions

433 Geostationary satellite observations of aerosol optical depth (AOD) over East Asia may usefully complement $PM_{2.5}$
 434 air quality networks if the local relationship between AOD and $PM_{2.5}$ can be inferred from a physical and/or

435 statistical model. Here we analyzed the ability of the GEOS-Chem chemical transport model to provide this
436 relationship by using a new fused GOCI/AHI geostationary satellite product together with AERONET ground-based
437 AOD measurements, aerosol vertical profiles over South Korea from the KORUS-AQ aircraft campaign (May-June
438 2016), and surface network observations. This allowed us to identify the critical features and limitations of the
439 model for successful representing the AOD-PM_{2.5} relationship.

440 The KORUS-AQ observations show that total aerosol extinction (550 nm) in the vertical column is dominated by
441 sulfate-nitrate-ammonium (SNA) and organic aerosol in the planetary boundary layer (PBL), despite large
442 concentrations of dust in the free troposphere. This reflects the optically effective size and high hygroscopicity of
443 the PBL aerosols. We find that GEOS-Chem aerosol optical properties based on measurements over the North
444 America (default model setting) underestimate KORUS-AQ aerosol mass extinction efficiency by around 20%. In
445 addition, a low bias in GEOS-FP RH below 1 km leads to a 10% underestimate of AOD inferred from the aircraft
446 profile. Adjustments of GEOS-Chem aerosol optical properties and RH enable a successful simulation of the aerosol
447 extinction profile. SNA aerosol contributes 59% of column aerosol extinction in the KORUS-AQ data, while
448 organic aerosol contributes 27% and dust contributes 12%.

449 Comparison of GOCI/AHI geostationary (GEO) satellite AOD to AERONET AODs over South Korea shows good
450 agreement, with high values along the west coast. GEOS-Chem is more consistent with the fine-mode AERONET
451 AOD because of its insufficient accounting of coarse particles, which account for 13% of AERONET AOD. The
452 remaining 15% underestimate of AERONET fine-mode AOD by GEOS-Chem can be attributed to the RH low bias.
453 GEOS-Chem overestimates 24-h surface PM_{2.5} over South Korea by 43% during the KORUS-AQ period, despite its
454 successful simulation of the aircraft data and fine-mode AERONET AOD, and we find that this is due to a large
455 overestimate of nighttime nitrate.

456 Broader examination of the GOCI/AHI AOD satellite data over East Asia shows spatial distributions and
457 magnitudes consistent with AERONET and featuring in particular strong Asian outflow in spring that includes a
458 large dust component. We find that AODs and PM_{2.5} have similar large-scale spatial distributions but opposite
459 seasonality. PM_{2.5} in North China has a strong winter maximum and summer minimum, while AOD shows the
460 opposite. GEOS-Chem simulates successfully the seasonality of measured PM_{2.5} but is ~ 20% biased low in summer
461 for AOD, due again to RH low bias like that during KORUS-AQ, amplified by the high RH in summer that drives
462 hygroscopic growth (Latimer and Martin, 2019). We find that the opposite AOD and PM_{2.5} seasonality is mainly
463 driven by residential coal heating sources and low PBL depths in winter, and high RH in summer. Observations of
464 PM_{2.5} and AOD in South Korea show the same seasonal phases as in North China but with much weaker amplitude,
465 reflecting the lack of residential coal burning in winter and a weaker seasonal amplitude of PBL depth.

466 In summary, we find that the geostationary GOCI/AHI satellite AOD data provide high-quality information for
467 monitoring of PM_{2.5} over East Asia but that physical interpretation requires accurate information on aerosol size
468 distributions, PBL depths, RH, the role of coarse particles, and diurnal variation of PM_{2.5}, all of which are subject to
469 large uncertainties in chemical transport models. Addressing these uncertainties should be a target of future work.

470 We have used results from our study in a recent machine-learning reconstruction of daily 2011-present PM_{2.5} over
471 East Asia from GOCI AOD data by identifying critical variables for the machine-learning algorithm and providing
472 blended gap-filling data for cloudy scenes (Pendergrass et al., 2021). Besides the factors discussed in this study,
473 topography might be another important factor influencing surface PM_{2.5} and its vertical mixing (Su et al., 2018), and
474 this also requires future investigation.

475

476 *Data availability.* Aircraft data during KORUS-AQ are available at: [www-air.larc.nasa.gov/cgi-](http://www-air.larc.nasa.gov/cgi-bin/ArcView/korusaq)
477 [bin/ArcView/korusaq](http://www-air.larc.nasa.gov/cgi-bin/ArcView/korusaq). PM_{2.5} data over China are from: quotsoft.net/air/. PM_{2.5} data over South Korea are from:
478 www.airkorea.or.kr/web. AERONET data can be found at: aeronet.gsfc.nasa.gov. The MEIC emission inventory are
479 at: www.meicmodel.org/. The KORUSv5 emission inventory is developed by Konkuk University, available at:
480 http://aisl.konkuk.ac.kr/#/emission_data/korus-aq_emissions.

481

482 *Author contributions.* SZ and DJJ designed the study. SZ performed the data analysis and model simulations with
483 contributions from JFB, KL, HCL, SKK, XW, PL, KRT, and Hong Liao. JK, SL, and Hyunkwang Lim provided
484 satellite AOD data. RJP and JIJ contributed to AirKorea data processing. JM and RM provided the dust emission
485 inventory. GL, FY, and JMM updated wet deposition simulation. JWH, BEA, JED, JLJ, PCJ, and BAN contributed
486 to KORUS-AQ campaign measurements. JHW and YK provided the KORUSv5 emission inventory. QZ provided
487 the MEIC emission inventory. SZ and DJJ wrote the paper with input from all authors.

488

489 *Acknowledgement.* This work was funded by the Samsung Advanced Institute of Technology and the Harvard-
490 NUIST Joint Laboratory for Air Quality and Climate (JLAQC). JLJ, PCJ, and BAN acknowledge NASA grant
491 NNX15AT96G and 80NSSC19K0124 for support.

492

493 *Competing interests.* The authors declare that they have no conflict of interest.

494

495 **References**

496 Alexander, B., Park Rokjin, J., Jacob Daniel, J., and Gong, S.: Transition metal-catalyzed oxidation of atmospheric
497 sulfur: Global implications for the sulfur budget, *J. Geophys. Res. Atmos.*, 114, D02309,
498 <https://doi.org/10.1029/2008JD010486>, 2009.

499 Amos, H. M., Jacob, D. J., Holmes, C. D., Fisher, J. A., Wang, Q., Yantosca, R. M., Corbitt, E. S., Galarneau, E.,
500 Rutter, A. P., Gustin, M. S., Steffen, A., Schauer, J. J., Graydon, J. A., Louis, V. L. S., Talbot, R. W., Edgerton, E.
501 S., Zhang, Y., and Sunderland, E. M.: Gas-particle partitioning of atmospheric Hg(II) and its effect on global
502 mercury deposition, *Atmos. Chem. Phys.*, 12, 591-603, <https://doi.org/10.5194/acp-12-591-2012>, 2012.

503 Brauer, M., Freedman, G., Frostad, J., van Donkelaar, A., Martin, R. V., Dentener, F., Dingenen, R. v., Estep, K.,
504 Amini, H., Apte, J. S., Balakrishnan, K., Barregard, L., Broday, D., Feigin, V., Ghosh, S., Hopke, P. K., Knibbs, L.
505 D., Kokubo, Y., Liu, Y., Ma, S., Morawska, L., Sangrador, J. L. T., Shaddick, G., Anderson, H. R., Vos, T.,
506 Forouzanfar, M. H., Burnett, R. T., and Cohen, A.: Ambient Air Pollution Exposure Estimation for the Global
507 Burden of Disease 2013, *Environ. Sci. Technol.*, 50, 79-88, [10.1021/acs.est.5b03709](https://doi.org/10.1021/acs.est.5b03709), 2016.

508 Brock, C. A., Wagner, N. L., Anderson, B. E., Beyersdorf, A., Campuzano-Jost, P., Day, D. A., Diskin, G. S.,
509 Gordon, T. D., Jimenez, J. L., Lack, D. A., Liao, J., Markovic, M. Z., Middlebrook, A. M., Perring, A. E.,
510 Richardson, M. S., Schwarz, J. P., Welti, A., Ziemba, L. D., and Murphy, D. M.: Aerosol optical properties in the
511 southeastern United States in summer – Part 2: Sensitivity of aerosol optical depth to relative humidity and aerosol
512 parameters, *Atmos. Chem. Phys.*, 16, 5009-5019, [10.5194/acp-16-5009-2016](https://doi.org/10.5194/acp-16-5009-2016), 2016.

513 Chen, G., Li, S., Knibbs, L. D., Hamm, N. A. S., Cao, W., Li, T., Guo, J., Ren, H., Abramson, M. J., and Guo, Y.: A
514 machine learning method to estimate PM_{2.5} concentrations across China with remote sensing, meteorological and
515 land use information, *Sci. Total Environ.*, 636, 52-60, <https://doi.org/10.1016/j.scitotenv.2018.04.251>, 2018.

516 Chen, W., Tang, H., and Zhao, H.: Diurnal, weekly and monthly spatial variations of air pollutants and air quality of
517 Beijing, *Atmos. Environ.*, 119, 21-34, <https://doi.org/10.1016/j.atmosenv.2015.08.040>, 2015.

518 Cheng, Y., Dai, T., Goto, D., Schutgens, N. A. J., Shi, G., and Nakajima, T.: Investigating the assimilation of
519 CALIPSO global aerosol vertical observations using a four-dimensional ensemble Kalman filter, *Atmos. Chem.
520 Phys.*, 19, 13445-13467, <https://doi.org/10.5194/acp-19-13445-2019>, 2019.

521 Chin, M., Ginoux, P., Kinne, S., Torres, O., Holben, B. N., Duncan, B. N., Martin, R. V., Logan, J. A., Higurashi,
522 A., and Nakajima, T.: Tropospheric Aerosol Optical Thickness from the GOCART Model and Comparisons with
523 Satellite and Sun Photometer Measurements, *J. Atmos. Sci.*, 59, 461-483, [https://doi.org/10.1175/1520-0469\(2002\)059<0461:TAOTFT>2.0.CO;2](https://doi.org/10.1175/1520-0469(2002)059<0461:TAOTFT>2.0.CO;2), 2002.

525 Choi, M., Kim, J., Lee, J., Kim, M., Park, Y. J., Holben, B., Eck, T. F., Li, Z., and Song, C. H.: GOCI Yonsei
526 aerosol retrieval version 2 products: an improved algorithm and error analysis with uncertainty estimation from 5-
527 year validation over East Asia, *Atmos. Meas. Tech.*, 11, 385-408, [10.5194/amt-11-385-2018](https://doi.org/10.5194/amt-11-385-2018), 2018.

528 Choi, J., Park, R. J., Lee, H.-M., Lee, S., Jo, D. S., Jeong, J. I., Henze, D. K., Woo, J.-H., Ban, S.-J., Lee, M.-D.,
529 Lim, C.-S., Park, M.-K., Shin, H. J., Cho, S., Peterson, D., and Song, C.-K.: Impacts of local vs. trans-boundary
530 emissions from different sectors on PM_{2.5} exposure in South Korea during the KORUS-AQ campaign, *Atmos.
531 Environ.*, 203, 196-205, <https://doi.org/10.1016/j.atmosenv.2019.02.008>, 2019.

532 Choi, M., Kim, J., Lee, J., Kim, M., Park, Y. J., Jeong, U., Kim, W., Hong, H., Holben, B., Eck, T. F., Song, C. H.,
533 Lim, J. H., and Song, C. K.: GOCI Yonsei Aerosol Retrieval (YAER) algorithm and validation during the
534 DRAGON-NE Asia 2012 campaign, *Atmos. Meas. Tech.*, 9, 1377-1398, <https://doi.org/10.5194/amt-9-1377-2016>,
535 2016.

536 Crawford, J. H., Ahn, J. Y., Al-Saadi, J., Chang, L., Emmons, L., Kim, J., Lee, G., Park, J. H., Park, R., Woo, J. H.,
537 Song, C. K., Hong, J.-H., Hong, Y.-D., Lefer, B. L., Lee, M., Lee, T., Kim, S., Min, K.-E., Yum, S. S., Shin, H. J.,
538 Kim, Y.-W., Choi, J.-S., Park, J.-S., Szykman, J. J., Long, R. W., Jordan, C. E., Simpson, I. J., Fried, A., Dibb, J. E.,
539 Cho, S. Y., and Kim, Y. P.: The Korea-United States air quality (KORUS-AQ) field study, *Elementa-Sci. Anthropol.*,
540 in press, 2021.

541 Curci, G.: FlexAOD: a chemistry-transport model post-processing tool for a flexible calculation of aerosol optical
542 properties, 1-4, http://pumpkin.aquila.infn.it/gabri/download/curci_istp2012.pdf, 2012.

543 Dai, Q., Bi, X., Liu, B., Li, L., Ding, J., Song, W., Bi, S., Schulze, B. C., Song, C., Wu, J., Zhang, Y., Feng, Y., and
544 Hopke, P. K.: Chemical nature of PM_{2.5} and PM₁₀ in Xi'an, China: Insights into primary emissions and secondary
545 particle formation, *Environmental Pollution*, 240, 155-166, <https://doi.org/10.1016/j.envpol.2018.04.111>, 2018.

546 Di, Q., Amini, H., Shi, L., Kloog, I., Silvern, R., Kelly, J., Sabath, M. B., Choirat, C., Koutrakis, P., Lyapustin, A.,
547 Wang, Y., Mickley, L. J., and Schwartz, J.: An ensemble-based model of PM_{2.5} concentration across the contiguous
548 United States with high spatiotemporal resolution, *Environ. Int.*, 130, 104909,
549 <https://doi.org/10.1016/j.envint.2019.104909>, 2019.

550 Dibb, J. E., Talbot, R. W., Scheuer, E. M., Seid, G., Avery, M. A., and Singh, H. B.: Aerosol chemical composition
551 in Asian continental outflow during the TRACE-P campaign: Comparison with PEM-West B, *J. Geophys. Res.*
552 *Atmos.*, 108, 8815, <https://doi.org/10.1029/2002JD003111>, 2003.

553 Fairlie, T. D., Jacob, D. J., and Park, R. J.: The impact of transpacific transport of mineral dust in the United States,
554 *Atmos. Environ.*, 41, 1251-1266, <https://doi.org/10.1016/j.atmosenv.2006.09.048>, 2007.

555 Fairlie, T. D., Jacob, D. J., Dibb, J. E., Alexander, B., Avery, M. A., van Donkelaar, A., and Zhang, L.: Impact of
556 mineral dust on nitrate, sulfate, and ozone in transpacific Asian pollution plumes, *Atmos. Chem. Phys.*, 10, 3999-
557 4012, <https://doi.org/10.5194/acp-10-3999-2010>, 2010.

558 Fisher, J. A., Jacob, D. J., Wang, Q., Bahreini, R., Carouge, C. C., Cubison, M. J., Dibb, J. E., Diehl, T., Jimenez, J.
559 L., Leibensperger, E. M., Lu, Z., Meinders, M. B. J., Pye, H. O. T., Quinn, P. K., Sharma, S., Streets, D. G., van
560 Donkelaar, A., and Yantosca, R. M.: Sources, distribution, and acidity of sulfate–ammonium aerosol in the Arctic in
561 winter–spring, *Atmos. Environ.*, 45, 7301-7318, <https://doi.org/10.1016/j.atmosenv.2011.08.030>, 2011.

562 Fountoukis, C. and Nenes, A.: ISORROPIA II: a computationally efficient thermodynamic equilibrium model for
563 $K^+Ca^{2+}Mg^{2+}NH_4^+Na^+SO_4^{2-}NO_3^-Cl^-H_2O$ aerosols, *Atmos. Chem. Phys.*, 7, 4639-4659,
564 <https://doi.org/10.5194/acp-7-4639-2007>, 2007.

565 Geng, G., Zhang, Q., Tong, D., Li, M., Zheng, Y., Wang, S., and He, K.: Chemical composition of ambient $PM_{2.5}$
566 over China and relationship to precursor emissions during 2005-2012, *Atmos. Chem. Phys.*, 17, 9187–9203,
567 <https://doi.org/10.5194/acp-17-9187-2017>, 2017.

568 Giles, D. M., Sinyuk, A., Sorokin, M. G., Schafer, J. S., Smirnov, A., Slutsker, I., Eck, T. F., Holben, B. N., Lewis,
569 J. R., Campbell, J. R., Welton, E. J., Korokin, S. V., and Lyapustin, A. I.: Advancements in the Aerosol Robotic
570 Network (AERONET) Version 3 database - automated near-real-time quality control algorithm with improved cloud
571 screening for Sun photometer aerosol optical depth (AOD) measurements, *Atmos. Meas. Tech.*, 12, 169-209,
572 <https://doi.org/10.5194/amt-12-169-2019>, 2019.

573 Guenther, A. B., Jiang, X., Heald, C. L., Sakulyanontvittaya, T., Duhl, T., Emmons, L. K., and Wang, X.: The
574 Model of Emissions of Gases and Aerosols from Nature version 2.1 (MEGAN2. 1): an extended and updated
575 framework for modeling biogenic emissions, *Geosci. Model Dev.*, 5, 1471-1492, <https://doi.org/10.5194/gmd-5-1471-2012>, 2012.

577 Guo, J., Xia, F., Zhang, Y., Liu, H., Li, J., Lou, M., He, J., Yan, Y., Wang, F., Min, M., and Zhai, P.: Impact of
578 diurnal variability and meteorological factors on the $PM_{2.5}$ - AOD relationship: Implications for $PM_{2.5}$ remote
579 sensing, *Environ. Pollut.*, 221, 94-104, <https://doi.org/10.1016/j.envpol.2016.11.043>, 2017.

580 Guo, H., Campuzano-Jost, P., Nault, B. A., Day, D. A., Schroder, J. C., Dibb, J. E., Dollner, M., Weinzierl, B., and
581 Jimenez, J. L.: The Importance of Size Ranges in Aerosol Instrument Intercomparisons: A Case Study for the ATom
582 Mission, *Atmos. Meas. Tech. Discuss.*, 2020, 1-49, <https://doi.org/10.5194/amt-2020-224>, 2020.

583 Hair, J. W., Hostetler, C. A., Cook, A. L., Harper, D. B., Ferrare, R. A., Mack, T. L., Welch, W., Izquierdo, L. R.,
584 and Hovis, F. E.: Airborne High Spectral Resolution Lidar for profiling aerosol optical properties, *Appl. Opt.*, 47,
585 6734-6752, <https://doi.org/10.1364/AO.47.006734>, 2008.

586 Hammer, M. S., van Donkelaar, A., Li, C., Lyapustin, A., Sayer, A. M., Hsu, N. C., Levy, R. C., Garay, M.,
587 Kalashnikova, O., Kahn, R. A., Brauer, M., Apte, J. S., Henze, D. K., Zhang, L., Zhang, Q., Ford, B., Pierce, J. R.,
588 and Martin, R. V.: Global Estimates and Long-Term Trends of Fine Particulate Matter Concentrations (1998-2018),
589 *Environ. Sci. Technol.*, 54, 7879-7890, <https://dx.doi.org/10.1021/acs.est.0c01764>, 2020.

590 Hu, X., Belle, J. H., Meng, X., Wildani, A., Waller, L. A., Strickland, M. J., and Liu, Y.: Estimating $PM_{2.5}$
591 Concentrations in the Conterminous United States Using the Random Forest Approach, *Environ. Sci. Technol.*, 51,
592 6936-6944, [10.1021/acs.est.7b01210](https://doi.org/10.1021/acs.est.7b01210), 2017.

593 Hudman, R. C., Moore, N. E., Mebust, A. K., Martin, R. V., Russell, A. R., Valin, L. C., and Cohen, R. C.: Steps
594 towards a mechanistic model of global soil nitric oxide emissions: implementation and space based-constraints,
595 *Atmos. Chem. Phys.*, 12, 7779-7795, <https://doi.org/10.5194/acp-12-7779-2012>, 2012.

596 Jaeglé, L., Quinn, P. K., Bates, T. S., Alexander, B., and Lin, J. T.: Global distribution of sea salt aerosols: new
597 constraints from in situ and remote sensing observations, *Atmos. Chem. Phys.*, 11, 3137-3157,
598 <https://doi.org/10.5194/acp-11-3137-2011>, 2011.

599 Jaeglé, L., Shah, V., Thornton, J. A., Lopez-Hilfiker, F. D., Lee, B. H., McDuffie, E. E., Fibiger, D., Brown, S. S.,
600 Veres, P., Sparks, T. L., Ebben, C. J., Wooldridge, P. J., Kenagy, H. S., Cohen, R. C., Weinheimer, A. J., Campos,
601 T. L., Montzka, D. D., Digangi, J. P., Wolfe, G. M., Hanisco, T., Schroder, J. C., Campuzano-Jost, P., Day, D. A.,
602 Jimenez, J. L., Sullivan, A. P., Guo, H., and Weber, R. J.: Nitrogen Oxides Emissions, Chemistry, Deposition, and
603 Export Over the Northeast United States During the WINTER Aircraft Campaign, *J. Geophys. Res. Atmos.*, 123,
604 12,368-312,393, <https://doi.org/10.1029/2018JD029133>, 2018.

605 Jeong, J. I., Park, R. J., and Youn, D.: Effects of Siberian forest fires on air quality in East Asia during May 2003
606 and its climate implication, *Atmos. Environ.*, 42, 8910-8922, <https://doi.org/10.1016/j.atmosenv.2008.08.037>, 2008.

607 Jordan, C. E., Crawford, J. H., Beyersdorf, A. J., Eck, T. F., Halliday, H. S., Nault, B. A., Chang, L.-S., Park, J.,
608 Park, R., and Lee, G.: Investigation of factors controlling PM_{2.5} variability across the South Korean Peninsula during
609 KORUS-AQ, *Elementa-Sci. Anthropol.*, 8, 28, <https://doi.org/10.1525/elementa.424>, 2020.

610 Kim, H., Zhang, Q., and Heo, J.: Influence of intense secondary aerosol formation and long-range transport on
611 aerosol chemistry and properties in the Seoul Metropolitan Area during spring time: results from KORUS-AQ,
612 *Atmos. Chem. Phys.*, 18, 7149-7168, <https://doi.org/10.5194/acp-18-7149-2018>, 2018.

613 Kumar, R., Delle Monache, L., Bresch, J., Saide, P. E., Tang, Y., Liu, Z., da Silva, A. M., Alessandrini, S., Pfister,
614 G., Edwards, D., Lee, P., and Djalalova, I.: Toward Improving Short-Term Predictions of Fine Particulate Matter
615 Over the United States Via Assimilation of Satellite Aerosol Optical Depth Retrievals, *J. Geophys. Res. Atmos.*,
616 124, 2753-2773, <https://doi.org/10.1029/2018JD029009>, 2019.

617 Lamb, K. D., Perring, A. E., Samset, B., Peterson, D., Davis, S., Anderson, B. E., Beyersdorf, A., Blake, D. R.,
618 Campuzano-Jost, P., Corr, C. A., Diskin, G. S., Kondo, Y., Moteki, N., Nault, B. A., Oh, J., Park, M., Pusede, S. E.,
619 Simpson, I. J., Thornhill, K. L., Wisthaler, A., and Schwarz, J. P.: Estimating Source Region Influences on Black
620 Carbon Abundance, Microphysics, and Radiative Effect Observed Over South Korea, *J. Geophys. Res. Atmos.*, 123,
621 13,527-513,548, <https://doi.org/10.1029/2018JD029257>, 2018.

622 Latimer, R. N. C. and Martin, R. V.: Interpretation of measured aerosol mass scattering efficiency over North
623 America using a chemical transport model, *Atmos. Chem. Phys.*, 19, 2635-2653, <https://doi.org/10.5194/acp-19-2635-2019>, 2019.

625 Lee, W., Lim, T., and Kim, D. D.: Thermal and Energy Performance Assessment of the Prefab Electric Ondol
626 System for Floor Heating in a Residential Building, *Energies*, 13, 5723, <https://doi.org/10.3390/en13215723>, 2020.

627 Lennartson, E. M., Wang, J., Gu, J., Castro Garcia, L., Ge, C., Gao, M., Choi, M., Saide, P. E., Carmichael, G. R.,
628 Kim, J., and Janz, S. J.: Diurnal variation of aerosol optical depth and PM_{2.5} in South Korea: a synthesis from
629 AERONET, satellite (GOCI), KORUS-AQ observation, and the WRF-Chem model, *Atmos. Chem. Phys.*, 18,
630 15125-15144, [10.5194/acp-18-15125-2018](https://doi.org/10.5194/acp-18-15125-2018), 2018.

631 Li, K., Liao, H., Zhu, J., and Moch Jonathan, M.: Implications of RCP emissions on future PM_{2.5} air quality and
632 direct radiative forcing over China, *J. Geophys. Res. Atmos.*, 121, 12,985-913,008,
633 <https://doi.org/10.1002/2016JD025623>, 2016.

634 Lim, H., Choi, M., Kim, J., Kasai, Y., and Chan, P.: AHI/Himawari-8 Yonsei Aerosol Retrieval (YAER):
635 Algorithm, Validation and Merged Products, *Remote Sens.*, 10, 699, <https://doi.org/10.3390/rs10050699>, 2018.

636 Lim, H., Go, S., Kim, J., Choi, M., Lee, S., Song, C. K., and Kasai, Y.: Integration of GOCI and AHI Yonsei aerosol
637 optical depth products during the 2016 KORUS-AQ and 2018 EMeRGe campaigns, *Atmos. Meas. Tech.*, 14, 4575-
638 4592, [10.5194/amt-14-4575-2021](https://doi.org/10.5194/amt-14-4575-2021), 2021.

639 Lin, J. and McElroy, M. B.: Impacts of boundary layer mixing on pollutant vertical profiles in the lower
640 troposphere: Implications to satellite remote sensing, *Atmos. Environ.*, 44, 1726-1739,
641 <https://doi.org/10.1016/j.atmosenv.2010.02.009>, 2010.

642 Liu, H., Jacob, D. J., Bey, I., and Yantosca, R. M.: Constraints from ²¹⁰Pb and ⁷Be on wet deposition and transport in
643 a global three-dimensional chemical tracer model driven by assimilated meteorological fields, *J. Geophys. Res.*
644 *Atmos.*, 106, 12109-12128, <https://doi.org/10.1029/2000JD900839>, 2001.

645 Liu, H., Jacob Daniel, J., Bey, I., Yantosca Robert, M., Duncan Bryan, N., and Sachse Glen, W.: Transport pathways
646 for Asian pollution outflow over the Pacific: Interannual and seasonal variations, *J. Geophys. Res. Atmos.*, 108,
647 8786, <https://doi.org/10.1029/2002JD003102>, 2003.

648 Liu, P., Zhao, C., Liu, P., Deng, Z., Huang, M., Ma, X., and Tie, X.: Aircraft study of aerosol vertical distributions
649 over Beijing and their optical properties, *Tellus B Chem. Phys. Meteorol.*, 61, 756-767, 10.1111/j.1600-
650 0889.2009.00440.x, 2009.

651 Liu, Y., Park, R. J., Jacob, D. J., Li, Q., Kilaru, V., and Sarnat, J. A.: Mapping annual mean ground-level PM_{2.5}
652 concentrations using Multiangle Imaging Spectroradiometer aerosol optical thickness over the contiguous United
653 States, *J. Geophys. Res. Atmos.*, 109, D22206, <https://doi.org/10.1029/2004JD005025>, 2004.

654 Luo, G., Yu, F., and Moch, J. M.: Further improvement of wet process treatments in GEOS-Chem v12.6.0: impact
655 on global distributions of aerosols and aerosol precursors, *Geosci. Model Dev.*, 13, 2879-2903,
656 <https://doi.org/10.5194/gmd-13-2879-2020>, 2020.

657 Luo, G., Yu, F., and Schwab, J.: Revised treatment of wet scavenging processes dramatically improves GEOS-Chem
658 12.0.0 simulations of nitric acid, nitrate, and ammonium over the United States, *Geosci. Model Dev.*, 12, 3439-3447
659 <https://doi.org/10.5194/gmd-12-3439-2019>, 2019.

660 Martin, R. V., Jacob, D. J., Yantosca, R. M., Chin, M., and Ginoux, P.: Global and regional decreases in
661 tropospheric oxidants from photochemical effects of aerosols, *J. Geophys. Res. Atmos.*, 108, 4097,
662 <https://doi.org/10.1029/2002JD002622>, 2003.

663 McNaughton, C. S., Clarke, A. D., Howell, S. G., Pinkerton, M., Anderson, B., Thornhill, L., Hudgins, C.,
664 Winstead, E., Dibb, J. E., Scheuer, E., and Maring, H.: Results from the DC-8 Inlet Characterization Experiment
665 (DICE): Airborne Versus Surface Sampling of Mineral Dust and Sea Salt Aerosols, *Aerosol Sci. Tech.*, 41, 136-159,
666 <https://doi.org/10.1080/02786820601118406>, 2007.

667 McNaughton, C. S., Clarke, A. D., Kapustin, V., Shinozuka, Y., Howell, S. G., Anderson, B. E., Winstead, E., Dibb,
668 J., Scheuer, E., Cohen, R. C., Wooldridge, P., Perring, A., Huey, L. G., Kim, S., Jimenez, J. L., Dunlea, E. J.,
669 DeCarlo, P. F., Wennberg, P. O., Crouse, J. D., Weinheimer, A. J., and Flocke, F.: Observations of heterogeneous
670 reactions between Asian pollution and mineral dust over the Eastern North Pacific during INTEX-B, *Atmos. Chem.*
671 *Phys.*, 9, 8283-8308, <https://doi.org/10.5194/acp-9-8283-2009>, 2009.

672 Meng, J., Martin, R. V., Ginoux, P., Hammer, M., Sulprizio, M. P., Ridley, D. A., and van Donkelaar, A.: Grid-
673 independent High Resolution Dust Emissions (v1.0) for Chemical Transport Models: Application to GEOS-Chem
674 (version 12.5.0), *Geosci. Model Dev. Discuss.*, 1-23, <https://doi.org/10.5194/gmd-2020-380>, 2020.

675 Miao, R., Chen, Q., Zheng, Y., Cheng, X., Sun, Y., Palmer, P. I., Shrivastava, M., Guo, J., Zhang, Q., Liu, Y., Tan,
676 Z., Ma, X., Chen, S., Zeng, L., Lu, K., and Zhang, Y.: Model bias in simulating major chemical components of
677 PM_{2.5} in China, *Atmos. Chem. Phys.*, 20, 12265-12284, <https://doi.org/10.5194/acp-20-12265-2020>, 2020.

678 Murray, L. T., Jacob, D. J., Logan, J. A., Hudman, R. C., and Koshak, W. J.: Optimized regional and interannual
679 variability of lightning in a global chemical transport model constrained by LIS/OTD satellite data, *J. Geophys. Res.*
680 *Atmos.*, 117, D20307, <https://doi.org/10.1029/2012JD017934>, 2012.

681 Nault, B. A., Campuzano-Jost, P., Day, D. A., Schroder, J. C., Anderson, B., Beyersdorf, A. J., Blake, D. R., Brune,
682 W. H., Choi, Y., Corr, C. A., de Gouw, J. A., Dibb, J., DiGangi, J. P., Diskin, G. S., Fried, A., Huey, L. G., Kim, M.
683 J., Knote, C. J., Lamb, K. D., Lee, T., Park, T., Pusede, S. E., Scheuer, E., Thornhill, K. L., Woo, J. H., and Jimenez,
684 J. L.: Secondary organic aerosol production from local emissions dominates the organic aerosol budget over Seoul,
685 South Korea, during KORUS-AQ, *Atmos. Chem. Phys.*, 18, 17769-17800, <https://doi.org/10.5194/acp-18-17769-2018>, 2018.

687 O'Neill, N. T., Eck, T. F., Smirnov, A., Holben, B. N., and Thulasiraman, S.: Spectral discrimination of coarse and
688 fine mode optical depth, *J. Geophys. Res. Atmos.*, 108, <https://doi.org/10.1029/2002JD002975>, 2003.

689 Pai, S. J., Heald, C. L., Pierce, J. R., Farina, S. C., Marais, E. A., Jimenez, J. L., Campuzano-Jost, P., Nault, B. A.,
690 Middlebrook, A. M., Coe, H., Shilling, J. E., Bahreini, R., Dingle, J. H., and Vu, K.: An evaluation of global organic
691 aerosol schemes using airborne observations, *Atmos. Chem. Phys.*, 20, 2637-2665, <https://doi.org/10.5194/acp-20-2637-2020>, 2020.

693 Park, R. J., Oak, Y. J., Emmons, L. K., Kim, C.-H., Pfister, G. G., Carmichael, G. R., Saide, P. E., Cho, S.-Y., Kim,
694 S., Woo, J.-H., Crawford, J. H., Gaubert, B., Lee, H.-J., Park, S.-Y., Jo, Y.-J., Gao, M., Tang, B., Stanier, C. O.,
695 Shin, S. S., Park, H. Y., Bae, C., and Kim, E.: Multi-model intercomparisons of air quality simulations for the
696 KORUS-AQ campaign, *Elementa-Sci. Anthropol.*, 9, 00139, <https://doi.org/10.1525/elementa.2021.00139>, 2021.

697 Park Rokjin, J., Jacob Daniel, J., Field Brendan, D., Yantosca Robert, M., and Chin, M.: Natural and transboundary
698 pollution influences on sulfate-nitrate-ammonium aerosols in the United States: Implications for policy, *J. Geophys.*
699 *Res. Atmos.*, 109, D15204, <https://doi.org/10.1029/2003JD004473>, 2004.

700 Pendergrass, D. C., Jacob, D. J., Zhai, S., Kim, J., Koo, J. H., Lee, S., Bae, M., Kim, S.: Continuous mapping of fine
701 particulate matter (PM_{2.5}) air quality in East Asia at daily 6x6 km² resolution by application of a random forest
702 algorithm to 2011-2019 GOCI geostationary satellite data, submitted, 2021.

703 Peterson, D. A., Hyer, E. J., Han, S.-O., Crawford, J. H., Park, R. J., Holz, R., Kuehn, R. E., Eloranta, E., Knote, C.,
704 Jordan, C. E., and Lefer, B. L.: Meteorology influencing springtime air quality, pollution transport, and visibility in
705 Korea, *Elementa-Sci. Anthropol.*, 7, 57, <https://doi.org/10.1525/elementa.395>, 2019.

706 Philip, S., Martin, R. V., Snider, G., Weagle, C. L., van Donkelaar, A., Brauer, M., Henze, D. K., Klimont, Z.,
707 Venkataraman, C., and Guttikunda, S. K.: Anthropogenic fugitive, combustion and industrial dust is a significant,
708 underrepresented fine particulate matter source in global atmospheric models, *Environ. Res. Lett.*, 12, 044018,
709 <https://doi.org/10.1088/1748-9326/aa65a4>, 2017.

710 Podolske, J. R., Sachse, G. W., and Diskin, G. S.: Calibration and data retrieval algorithms for the NASA
711 Langley/Ames Diode Laser Hygrometer for the NASA Transport and Chemical Evolution Over the Pacific
712 (TRACE-P) mission, *J. Geophys. Res. Atmos.*, 108, 8792, <https://doi.org/10.1029/2002JD003156>, 2003.

713 Pye, H. O. T., Liao, H., Wu, S., Mickley, L. J., Jacob, D. J., Henze, D. K., and Seinfeld, J. H.: Effect of changes in
714 climate and emissions on future sulfate-nitrate-ammonium aerosol levels in the United States, *J. Geophys. Res.*
715 *Atmos.*, 114, D01205, <https://doi.org/10.1029/2008JD010701>, 2009.

716 Qu, W., Wang, J., Zhang, X., Sheng, L., and Wang, W.: Opposite seasonality of the aerosol optical depth and the
717 surface particulate matter concentration over the north China Plain, *Atmos. Environ.*, 127, 90-99,
718 <https://doi.org/10.1016/j.atmosenv.2015.11.061>, 2016.

719 Saide, P. E., Kim, J., Song, C. H., Choi, M., Cheng, Y., and Carmichael, G. R.: Assimilation of next generation
720 geostationary aerosol optical depth retrievals to improve air quality simulations, *Geophys. Res. Lett.*, 41, 9188-9196,
721 <https://doi.org/10.1002/2014GL062089>, 2014.

722 Saide, P. E., Gao, M., Lu, Z., Goldberg, D. L., Streets, D. G., Woo, J. H., Beyersdorf, A., Corr, C. A., Thornhill, K.
723 L., Anderson, B., Hair, J. W., Nehrir, A. R., Diskin, G. S., Jimenez, J. L., Nault, B. A., Campuzano-Jost, P., Dibb, J.,
724 Heim, E., Lamb, K. D., Schwarz, J. P., Perring, A. E., Kim, J., Choi, M., Holben, B., Pfister, G., Hodzic, A.,
725 Carmichael, G. R., Emmons, L., and Crawford, J. H.: Understanding and improving model representation of aerosol
726 optical properties for a Chinese haze event measured during KORUS-AQ, *Atmos. Chem. Phys.*, 20, 6455-6478,
727 <https://doi.org/10.5194/acp-20-6455-2020>, 2020.

728 Scarino, A. J., Obland, M. D., Fast, J. D., Burton, S. P., Ferrare, R. A., Hostetler, C. A., Berg, L. K., Lefer, B.,
729 Haman, C., Hair, J. W., Rogers, R. R., Butler, C., Cook, A. L., and Harper, D. B.: Comparison of mixed layer
730 heights from airborne high spectral resolution lidar, ground-based measurements, and the WRF-Chem model during
731 CalNex and CARES, *Atmos. Chem. Phys.*, 14, 5547-5560, <https://doi.org/10.5194/acp-14-5547-2014>, 2014.

732 Sekiyama, T. T., Tanaka, T. Y., Shimizu, A., and Miyoshi, T.: Data assimilation of CALIPSO aerosol observations,
733 *Atmos. Chem. Phys.*, 10, 39-49, <https://doi.org/10.5194/acp-10-39-2010>, 2010.

734 Seinfeld, J. H. and Pandis, S. N.: *Atmospheric Chemistry and Physics: From Air Pollution to Climate Change*, Third
735 Edition, Ch. 8, John Wiley & Sons, New Jersey, 2016.

736 Shah, V., Jacob, D. J., Moch, J. M., Wang, X., and Zhai, S.: Global modeling of cloud water acidity, precipitation
737 acidity, and acid inputs to ecosystems, *Atmos. Chem. Phys.*, 20, 12223-12245, <https://doi.org/10.5194/acp-20-12223-2020>, 2020.

739 Su, T., Li, Z., and Kahn, R.: Relationships between the planetary boundary layer height and surface pollutants
740 derived from lidar observations over China: regional pattern and influencing factors, *Atmos. Chem. Phys.*, 18,
741 15921-15935, [10.5194/acp-18-15921-2018](https://doi.org/10.5194/acp-18-15921-2018), 2018.

742 Sun, X., Yin, Y., Sun, Y., Sun, Y., Liu, W., and Han, Y.: Seasonal and vertical variations in aerosol distribution over
743 Shijiazhuang, China, *Atmos. Environ.*, 81, 245-252, <https://doi.org/10.1016/j.atmosenv.2013.08.009>, 2013.

- 744 Travis, K. R., Crawford, J. H., Nault, B. A., Kim, H., Jordan, C. E., Chen, G., Zhai, S., Wang, X., Jimenez, J. L.,
745 Dibb, J. E., Brune, W. H., Weinheimer, A., Wennberg, P., Long, R., Szykman, J. J., Woo, J. H., Kim, Y., Li, K.,
746 McDuffie, E., Luo, G., Zhang, Q., Kim, S.: Why do models have difficulty simulating ammonium nitrate and nitric
747 acid in East Asia?, manuscript in preparation.
- 748 van Donkelaar, A., Martin Randall, V., Brauer, M., and Boys Brian, L.: Use of Satellite Observations for Long-
749 Term Exposure Assessment of Global Concentrations of Fine Particulate Matter, *Environ. Health Perspect.*, 123,
750 135-143, <https://doi.org/10.1289/ehp.1408646>, 2015.
- 751 van Donkelaar, A., Martin, R. V., Brauer, M., Hsu, N. C., Kahn, R. A., Levy, R. C., Lyapustin, A., Sayer, A. M., and
752 Winker, D. M.: Global Estimates of Fine Particulate Matter using a Combined Geophysical-Statistical Method with
753 Information from Satellites, Models, and Monitors, *Environ. Sci. Technol.*, 50, 3762-3772,
754 <https://doi.org/10.1021/acs.est.5b05833>, 2016.
- 755 van der Werf, G. R., Randerson, J. T., Giglio, L., van Leeuwen, T. T., Chen, Y., Rogers, B. M., Mu, M., van Marle,
756 M. J. E., Morton, D. C., Collatz, G. J., Yokelson, R. J., and Kasibhatla, P. S.: Global fire emissions estimates during
757 1997–2016, *Earth Syst. Sci. Data*, 9, 697-720, <https://doi.org/10.5194/essd-9-697-2017>, 2017.
- 758 van Donkelaar, A., Martin, R. V., Li, C., and Burnett, R. T.: Regional Estimates of Chemical Composition of Fine
759 Particulate Matter Using a Combined Geoscience-Statistical Method with Information from Satellites, Models, and
760 Monitors, *Environ. Sci. Technol.*, 53, 2595-2611, [10.1021/acs.est.8b06392](https://doi.org/10.1021/acs.est.8b06392), 2019.
- 761 van Donkelaar, A., Martin, R. V., and Park, R. J.: Estimating ground-level PM_{2.5} using aerosol optical depth
762 determined from satellite remote sensing, *J. Geophys. Res. Atmos.*, 111, [10.1029/2005JD006996](https://doi.org/10.1029/2005JD006996), 2006.
- 763 Wang, Q., Jacob, D. J., Fisher, J. A., Mao, J., Leibensperger, E. M., Carouge, C. C., Le Sager, P., Kondo, Y.,
764 Jimenez, J. L., Cubison, M. J., and Doherty, S. J.: Sources of carbonaceous aerosols and deposited black carbon in
765 the Arctic in winter-spring: implications for radiative forcing, *Atmos. Chem. Phys.*, 11, 12453-12473,
766 <https://doi.org/10.5194/acp-11-12453-2011>, 2011.
- 767 Wang, Q., Jacob, D. J., Spackman, J. R., Perring, A. E., Schwarz, J. P., Moteki, N., Marais, E. A., Ge, C., Wang, J.,
768 and Barrett, S. R. H.: Global budget and radiative forcing of black carbon aerosol: Constraints from pole-to-pole
769 (HIPPO) observations across the Pacific, *J. Geophys. Res. Atmos.*, 119, 195-206,
770 <https://doi.org/10.1002/2013JD020824>, 2014.
- 771 Wang, X., Heald, C. L., Ridley, D. A., Schwarz, J. P., Spackman, J. R., Perring, A. E., Coe, H., Liu, D., and Clarke,
772 A. D.: Exploiting simultaneous observational constraints on mass and absorption to estimate the global direct
773 radiative forcing of black carbon and brown carbon, *Atmos. Chem. Phys.*, 14, 10989-11010,
774 <https://doi.org/10.5194/acp-14-10989-2014>, 2014.
- 775 Wang, Y., Zhang, Q., Jiang, J., Zhou, W., Wang, B., He, K., Duan, F., Zhang, Q., Philip, S., and Xie, Y.: Enhanced
776 sulfate formation during China's severe winter haze episode in January 2013 missing from current models, *J.*
777 *Geophys. Res. Atmos.*, 119, 425-440, <https://doi.org/10.1002/2013JD021426>, 2014.
- 778 Wei, J., Li, Z., Lyapustin, A., Sun, L., Peng, Y., Xue, W., Su, T., and Cribb, M.: Reconstructing 1-km-resolution
779 high-quality PM_{2.5} data records from 2000 to 2018 in China: spatiotemporal variations and policy implications,
780 *Remote Sens. Environ.*, 252, 112136, <https://doi.org/10.1016/j.rse.2020.112136>, 2021.
- 781 Woo, J.-H., Kim, Y., Kim, H.-K., Choi, K.-C., Eum, J.-H., Lee, J.-B., Lim, J.-H., Kim, J., and Seong, M.:
782 Development of the CREATE Inventory in Support of Integrated Climate and Air Quality Modeling for Asia,
783 *Sustainability*, 12, 7930, <https://doi.org/10.3390/su12197930>, 2020.
- 784 Xiao, Q., Chang, H. H., Geng, G., and Liu, Y.: An Ensemble Machine-Learning Model To Predict Historical PM_{2.5}
785 Concentrations in China from Satellite Data, *Environ. Sci. Technol.*, 52, 13260-13269, [10.1021/acs.est.8b02917](https://doi.org/10.1021/acs.est.8b02917),
786 2018.
- 787 Xu, J., Han, F., Li, M., Zhang, Z., Xiaohui, D., and Wei, P.: On the opposite seasonality of MODIS AOD and
788 surface PM_{2.5} over the Northern China plain, *Atmos. Environ.*, 215, 116909,
789 <https://doi.org/10.1016/j.atmosenv.2019.116909>, 2019.
- 790 Xu, J. W., Martin, R. V., van Donkelaar, A., Kim, J., Choi, M., Zhang, Q., Geng, G., Liu, Y., Ma, Z., Huang, L.,
791 Wang, Y., Chen, H., Che, H., Lin, P., and Lin, N.: Estimating ground-level PM_{2.5} in eastern China using aerosol

792 optical depth determined from the GOCI satellite instrument, *Atmos. Chem. Phys.*, 15, 13133-13144, 10.5194/acp-
793 15-13133-2015, 2015.

794 Xue, T., Zheng, Y., Tong, D., Zheng, B., Li, X., Zhu, T., and Zhang, Q.: Spatiotemporal continuous estimates of
795 PM_{2.5} concentrations in China, 2000–2016: A machine learning method with inputs from satellites, chemical
796 transport model, and ground observations, *Environ. Int.*, 123, 345-357, <https://doi.org/10.1016/j.envint.2018.11.075>,
797 2019.

798 Zhai, S., Jacob, D. J., Wang, X., Shen, L., Li, K., Zhang, Y., Gui, K., Zhao, T., and Liao, H.: Fine particulate matter
799 (PM_{2.5}) trends in China, 2013-2018: separating contributions from anthropogenic emissions and meteorology,
800 *Atmos. Chem. Phys.*, 19, 11031-11041 <https://doi.org/10.5194/acp-19-11031-2019>, 2019.

801 Zhai, S., Jacob, D. J., Wang, X., Liu, Z., Wen, T., Shah, V., Li, K., Moch, J. M., Bates, K. H., Song, S., Shen, L.,
802 Zhang, Y., Luo, G., Yu, F., Sun, Y., Wang, L., Qi, M., Tao, J., Gui, K., Xu, H., Zhang, Q., Zhao, T., Wang, Y., Lee,
803 H. C., Choi, H., and Liao, H.: Control of particulate nitrate air pollution in China, *Nat. Geosci.*,
804 <https://doi.org/10.1038/s41561-021-00726-z>, 2021.

805 Zhang, L., Kok, J. F., Henze, D. K., Li, Q., and Zhao, C.: Improving simulations of fine dust surface concentrations
806 over the western United States by optimizing the particle size distribution, *Geophys. Res. Lett.*, 40, 3270-3275,
807 <https://doi.org/10.1002/grl.50591>, 2013.

808 Zhang, L., Gong, S., Padro, J., and Barrie, L.: A size-segregated particle dry deposition scheme for an atmospheric
809 aerosol module, *Atmos. Environ.*, 35, 549-560, [https://doi.org/10.1016/S1352-2310\(00\)00326-5](https://doi.org/10.1016/S1352-2310(00)00326-5), 2001.

810 Zhang, X., Wang, H., Che, H.-Z., Tan, S.-C., Shi, G.-Y., and Yao, X.-P.: The impact of aerosol on MODIS cloud
811 detection and property retrieval in seriously polluted East China, *Sci. Total Environ.*, 711, 134634,
812 <https://doi.org/10.1016/j.scitotenv.2019.134634>, 2020.

813 Zheng, B., Tong, D., Li, M., Liu, F., Hong, C., Geng, G., Li, H., Li, X., Peng, L., Qi, J., Yan, L., Zhang, Y., Zhao,
814 H., Zheng, Y., He, K., and Zhang, Q.: Trends in China's anthropogenic emissions since 2010 as the consequence of
815 clean air actions, *Atmos. Chem. Phys.*, 18, 14095-14111, <https://doi.org/10.5194/acp-18-14095-2018>, 2018.

816 Ziemba, L. D., Lee Thornhill, K., Ferrare, R., Barrick, J., Beyersdorf, A. J., Chen, G., Crumeyrolle, S. N., Hair, J.,
817 Hostetler, C., Hudgins, C., Obland, M., Rogers, R., Scarino, A. J., Winstead, E. L., and Anderson, B. E.: Airborne
818 observations of aerosol extinction by in situ and remote-sensing techniques: Evaluation of particle hygroscopicity,
819 *Geophys. Res. Lett.*, 40, 417-422, <https://doi.org/10.1029/2012GL054428>, 2013.

820